

# Globular Cluster Systems of Massive Compact Elliptical Galaxies in the Local Universe: Evidence for Relic Red Nuggets?

JISU KANG<sup>1</sup> AND MYUNG GYOON LEE<sup>1</sup>

<sup>1</sup>*Astronomy Program, Department of Physics and Astronomy, Seoul National University, 1 Gwanak-ro, Gwanak-gu, Seoul 08826, Republic of Korea*

(Received November 27, 2020; Accepted March 30, 2021)

Submitted to ApJ

## ABSTRACT

Nearby massive compact elliptical galaxies (MCEGs) are strong candidates for relic galaxies (i.e. local analogs of red nuggets at high redshifts). It is expected that the globular cluster (GC) systems of relic galaxies are dominated by red (metal-rich) GCs. NGC 1277 is known as a unique example of such a galaxy in the previous study. In this study, we search for GCs in 12 nearby MCEGs at distances of  $\lesssim 100$  Mpc from the Hubble Space Telescope/Wide Field Camera 3 F814W( $I_{814}$ )/F160W( $H_{160}$ ) archival images. We find that most of these MCEGs host a rich population of GCs with a color range of  $0.0 < (I_{814} - H_{160})_0 < 1.1$ . The fractions of their red GCs range from  $f_{RGC} = 0.2$  to  $0.7$  with a mean of  $f_{RGC} = 0.48 \pm 0.14$ . We divide the MCEG sample into two groups: one in clusters and the other in groups/fields. The mean red GC fraction of the cluster MCEGs is  $0.60 \pm 0.06$ , which is  $0.2$  larger than the value of the group/field MCEGs,  $0.40 \pm 0.10$ . The value for the cluster MCEGs is  $\sim 0.3$  larger than the mean value of giant early-type galaxies with similar stellar mass in the Virgo cluster ( $f_{RGC} = 0.33 \pm 0.13$ ). Our results show that most of the MCEGs in our sample are indeed relic galaxies. This further implies that a majority of the red GCs in MCEGs are formed early in massive galaxies and that most MCEGs in the local universe have rarely undergone mergers after they became red nuggets about 10 Gyr ago.

**Keywords:** Compact galaxies (285), Elliptical galaxies (456), Galaxy evolution (594), Globular star clusters (656)

## 1. INTRODUCTION

According to the current understanding of galaxy evolution, massive early-type galaxies (ETGs) form in two-phases (e.g. Khochfar & Silk 2006; van Dokkum et al. 2010; Oser et al. 2010, 2012; van der Wel et al. 2014; Wellons et al. 2016; Naab & Ostriker 2017; Toft et al. 2014, 2017, and references therein). They grow in size and mass from massive compact red progenitors through successive mergers. These progenitors are similar to ‘red nugget’ galaxies found at high redshift at  $z = 2 - 3$ . Red nugget galaxies are massive, compact, and composed of old stellar populations showing little evidence of recent star formation.

In the first phase of formation and evolution, red nugget galaxies might have underwent the following steps: (1) started with accretion-driven violent disc instability, leading to fast rotation; (2) contracted via dissipative process,

forming compact, star-forming blue nuggets; and (3) star formation in the blue nuggets quenched by feedback due to AGN activity. The blue nuggets became red nuggets about 10 Gyr ago (e.g. Dekel & Burkert 2014; Almaini et al. 2017; Tortora et al. 2018).

In the second phase of formation and evolution, most red nugget galaxies grow in size and mass by a number of minor mergers. They become larger ETGs with higher mass, as often seen in the local universe. According to deep observations of high redshift galaxies and simulations on size evolution, massive compact ETGs at  $z = 2 - 3$  have effective radii of  $\approx 1$  kpc and they grow by a factor of 5 to 6 in size until present day (e.g. Khochfar & Silk 2006; Oser et al. 2012; van der Wel et al. 2014; Furlong et al. 2017; Lapi et al. 2018).

However, if some of the red nuggets at high redshift rarely experience mergers during their evolution, they would appear as relic red nuggets in the local universe. Indeed, a small number of the relic red nugget candidates are found recently in the local universe (e.g. Yıldırım et al. 2017, and

Corresponding author: Myung Gyoon Lee  
jskang@astro.snu.ac.kr, mglee@astro.snu.ac.kr

references therein). These galaxies are good candidates for relic galaxies. Trujillo et al. (2014) defined a relic galaxy as “an object that was formed in the early phases of the universe (i.e.,  $z > 2$ ) and has remained unaltered (i.e., without significant gas or stellar accretion) since its initial formation”, and pointed out that these relic galaxies would appear today as “old massive galaxies which have the same structural properties as the population of massive galaxies at high- $z$ ” (i.e. old massive compact galaxies). Trujillo et al. (2014) suggested selection criteria for relic galaxy candidates in the local universe: old age ( $> 10$  Gyr), high stellar mass ( $M_* \gtrsim 10^{11} M_\odot$ ), and compact size ( $R_e \lesssim 1.5$  kpc).

There are several confirmed relic galaxies in the local universe. First, NGC 1277, a peculiar S0 galaxy at a distance of 73 Mpc in the Perseus cluster, has been confirmed as a relic galaxy (Trujillo et al. 2014). From the analysis of imaging and spectral data of the galaxy light, Trujillo et al. (2014) found that NGC 1277 is old ( $> 10$  Gyr), massive ( $M_* = 1.2 \pm 0.4 \times 10^{11} M_\odot$ ), and compact ( $R_e = 1.2$  kpc). They also estimated the metallicity of the central region in NGC 1277 to be above solar ( $[\text{Fe}/\text{H}] = 0.20 \pm 0.04$  and  $[\alpha/\text{Fe}] = 0.4 \pm 0.1$ ). NGC 1277 is rotating very quickly with a rotation velocity of  $v_{\text{rot}} \approx 300 \text{ km s}^{-1}$ , and it also shows a high central velocity dispersion of  $\sigma_v = 355 \text{ km s}^{-1}$  (Yildirim et al. 2017). Later, two more relic galaxies at distances of  $\lesssim 100$  Mpc, MRK 1216 and PGC 32873, were confirmed by Ferré-Mateu et al. (2017). They pointed out that these two galaxies host übermassive black holes (ÜMBH). They also inferred that these two galaxies have steep stellar initial mass function (IMF) profiles. Most recently, Spiniello et al. (2020) confirmed two more relic galaxies at intermediate redshift, KiDS J0224-3143 ( $z = 0.38$ ) and KiDS J0847+0112 ( $z = 0.18$ ).

Yildirim et al. (2017) presented a study of 16 compact elliptical galaxies thought to be good candidates for relic galaxies. These compact elliptical galaxies were selected from the Hobby-Eberly Telescope Massive Galaxy Survey (HETMGs; van den Bosch et al. 2015). This survey aims to find nearby galaxies that are suitable for a dynamical black hole mass measurement with high spatial resolution imaging follow-up. From the survey, 16 compact elliptical galaxies were selected with tight criteria in sphere-of-influence  $\geq 0''.05$  and  $R_e \leq 2$  kpc. The structural and dynamical properties of these selected galaxies were studied based on Hubble Space Telescope (HST) F160W images and wide-field integral field unit data. They are strong candidates for relic red nuggets in the sense that they follow the stellar mass–size relation for massive compact red galaxies at  $z \approx 2$ , while they show a significant deviation from the relation for massive ETGs in the local universe (Yildirim et al. 2017). Most have old ages ( $\gtrsim 10$  Gyr) and high metallicities above solar. NGC 1277, MRK 1216 and PGC 32873 are also included in the list of Yıldirim et al. (2017).

Although numerous studies have provided useful information about structural, photometric, and kinematic properties of the massive compact elliptical galaxies (MCEGs) from the analysis of their integrated galaxy light (e.g. Yıldirim et al. 2015, 2016, 2017, and references therein), much less is known about globular cluster (GC) systems in these galaxies. GCs are excellent tools to trace how their host galaxies evolve. In general, massive ETGs often host two subpopulations of GCs: blue (metal-poor) GCs and red (metal-rich) GCs (see Brodie & Strader 2006; Harris et al. 2017; Forbes & Remus 2018, and references therein). Red GCs are believed to have been formed in the progenitors of massive galaxies, while blue GCs are believed to have been formed in low mass galaxies and accreted to the massive galaxies through mergers (Brodie & Strader 2006; Lee et al. 2010a; Harris et al. 2017; Forbes & Remus 2018, and references therein).

The GCs in the Milky Way (MW) Galaxy are the best targets to estimate the ages of the GCs. The ages of the GCs in the MW Galaxy based on the recent isochrone fitting of the main sequences (e.g. Oliveira et al. 2020) range from 11.7 to 13.5 Gyrs, with a mean value of  $12.3 \pm 0.4$  Gyr. The mean age of the metal-rich (red) GCs ( $[\text{Fe}/\text{H}] > -0.85$ ),  $12.12 \pm 0.32$  Gyr, is slightly smaller than that of the metal-poor (blue) GCs ( $[\text{Fe}/\text{H}] < -0.85$ ),  $12.86 \pm 0.36$  Gyr. The age scatter in each subpopulation, as well as the age difference between the two subpopulations, is smaller than 1 Gyr, showing that they are formed almost simultaneously. Thus, the GCs are an efficient tracer of relic galaxies.

It is expected that GC systems in relic galaxies are dominated by red GCs if the relic galaxies have rarely undergone mergers after they became massive compact red galaxies at about 10 Gyr ago. Recently, from HST F475W( $g_{475}$ )/F850LP( $z_{850}$ ) photometry, Beasley et al. (2018) found that the GC system in NGC 1277 is dominated by red GCs (showing a red GC fraction of  $f_{\text{RGC}} > 83\%$ ), and they estimated that the total stellar mass accretion in this galaxy is minor ( $< 10\%$ ). From these results, they suggested that NGC 1277 is indeed a genuine relic galaxy. To date, NGC 1277 is the only MCEG whose GC system has been studied to estimate the red GC fraction.

In this study, we investigate GC systems in a large sample of nearby MCEGs. We expect to draw a conclusion whether the GC system of NGC 1277 is special or if most MCEGs follow NGC 1277 in the fraction of red GCs. The primary goals of this study are (1) to select GCs in each galaxy, (2) to estimate the fraction of red GCs in each galaxy, and (3) to investigate any differences in the GC systems (especially the fraction of the red GCs) between the MCEGs and the massive ETGs in the local universe.

We select target MCEGs from the list of 16 compact elliptical galaxies in Yıldirim et al. (2017). It is an excellent re-

**Table 1.** Basic Properties of the Target MCEGs and Reference Galaxies

Galaxy	$D$ [Mpc]	$R_{e,circ}$ [kpc]	$b/a$	$\sigma_c$ [km s $^{-1}$ ]	$\log(M_*/M_\odot)$	$B$ [mag]	$A_I$ and $A_H$	$f_{RGC}$
(1)	(2)	(3)	(4)	(5)	(6)	(7)	(8)	(9)
UGC 3816	$51 \pm 1$	$1.8 \pm 0.1$	0.69	$251 \pm 7$	$10.96^{+0.06}_{-0.04}$	13.46	0.095, 0.032	$0.51^{+0.12}_{-0.10}$
NGC 0384	$59 \pm 1$	$1.5 \pm 0.1$	0.68	$240 \pm 5$	$10.96^{+0.05}_{-0.05}$	13.67	0.096, 0.032	$0.45^{+0.08}_{-0.09}$
NGC 1281	$60 \pm 1$	$1.3 \pm 0.1$	0.64	$263 \pm 6$	$11.00^{+0.08}_{-0.08}$	13.74	0.256, 0.085	$0.70^{+0.09}_{-0.09}$
NGC 1270	$69 \pm 1$	$1.9 \pm 0.1$	0.68	$376 \pm 9$	$11.31^{+0.10}_{-0.12}$	13.43	0.253, 0.084	$0.61^{+0.06}_{-0.02}$
PGC 70520	$72 \pm 1$	$1.2 \pm 0.1$	0.49	$259 \pm 8$	$10.95^{+0.10}_{-0.12}$	14.17	0.147, 0.049	$0.30^{+0.07}_{-0.07}$
NGC 0472	$74 \pm 1$	$2.0 \pm 0.1$	0.72	$252 \pm 7$	$11.07^{+0.06}_{-0.11}$	13.73	0.075, 0.025	$0.41^{+0.12}_{-0.07}$
NGC 2767	$74 \pm 1$	$1.9 \pm 0.1$	0.75	$247 \pm 9$	$11.12^{+0.09}_{-0.08}$	14.36	0.029, 0.010	$0.37^{+0.01}_{-0.05}$
NGC 1271	$80 \pm 2$	$1.4 \pm 0.1$	0.43	$302 \pm 8$	$11.06^{+0.07}_{-0.07}$	14.30	0.254, 0.085	$0.60^{+0.05}_{-0.05}$
UGC 2698	$89 \pm 2$	$3.1 \pm 0.1$	0.73	$351 \pm 8$	$11.58^{+0.01}_{-0.03}$	13.61	0.224, 0.075	$0.56^{+0.04}_{-0.04}$
MRK 1216	$94 \pm 2$	$2.3 \pm 0.1$	0.58	$335 \pm 6$	$11.34^{+0.11}_{-0.10}$	14.44	0.050, 0.017	$0.52^{+0.09}_{-0.04}$
PGC 11179	$94 \pm 2$	$1.8 \pm 0.1$	0.66	$292 \pm 7$	$11.16^{+0.06}_{-0.08}$	14.51	0.287, 0.096	$0.56^{+0.03}_{-0.11}$
PGC 32873	$112 \pm 2$	$1.9 \pm 0.1$	0.53	$308 \pm 9$	$11.28^{+0.04}_{-0.04}$	14.98	0.019, 0.006	$0.24^{+0.06}_{-0.00}$
NGC 1399	20	11.1	0.91	$332 \pm 5$	11.41	10.60	0.019, 0.006	$0.72^{+0.06}_{-0.10}$
NGC 4874	100	22.7	0.87	$272 \pm 4$	11.76	12.63	0.014, 0.005	$0.55^{+0.08}_{-0.08}$

NOTE—(1) Galaxy name; (2) Distances; (3) Effective radii within circularized aperture; (4) The ratio of minor axis and major axis; (5) Central velocity dispersion; (6) Stellar mass derived from simple stellar population models for Salpeter-like stellar IMF (with a slope of  $\Gamma = 2.35$ ); (7) B-band magnitudes; (8) Foreground extinction for F814W( $I_{814}$ ) and F160W( $H_{160}$ ) bands; (9) Fractions of red GCs derived in this study ( $R < 10R_{e,circ}$  for the target MCEGs,  $R \lesssim 1R_e$  for NGC 1399 and  $R \lesssim 2R_e$  for NGC 4874)

**References**—(1–6) [Yildirim et al. \(2017\)](#) for the target MCEGs; (1,2,3,6) ACSFCS for NGC 1399, ACSFCS for NGC 4874; (4,5) HyperLeda for NGC 1399 and NGC 4874; (7) HyperLeda; (8) [Schlafly & Finkbeiner \(2011\)](#); (9) This study

source because HST F814W( $I_{814}$ )/F160W( $H_{160}$ ) images are available for most of them. From the list, we exclude NGC 3990, NGC 1282 and PGC 12562 because they have a stellar mass much lower than the other MCEGs. There are no F160W images available for NGC 1277 so we exclude it as well. Thus, we select 12 MCEGs as listed in Table 1. Basic properties of the target MCEGs given by [Yildirim et al. \(2017\)](#) are summarized in the table. The ranges of their physical parameters are: circularized effective radii of  $R_{e,circ} = 1.2$  to  $3.1$  kpc, central velocity dispersion of  $\sigma_c = 240$  to  $376$  km s $^{-1}$ , and stellar mass of  $\log(M_*/M_\odot) = 10.95$  to  $11.58$ .

After submitting this paper, [Alamo-Martínez et al. \(2021\)](#) presented a similar study of the MCEG GCs. They used the same MCEG targets as this work to study the general properties of the GCs in these galaxies, but they did not mention any subpopulations of the GCs. They did not provide any tables for the photometric data we can use for quantitative comparison, so we compared visually the color-magnitude diagrams (CMDs) and radial number density profiles of the GCs with [Alamo-Martínez et al. \(2021\)](#), finding that both are consistent with each other.

This paper is organized as follows. Section 2 describes the basic properties of the data, how we reduce the data, how we select GC candidates in each galaxy, and how we derive the total magnitudes and colors of the GC candidates. In Section

3 we present the CMDs and color distributions of the GCs in each galaxy, and how we estimate the fraction of red GCs in each galaxy. Then we show the spatial and radial distributions of the GCs in each galaxy. Section 4 discusses how the fractions of red GCs vary depending on sizes, magnitudes, and stellar masses of their host galaxies, and its implications on the origin of GCs and the evolution of MCEGs. Our results and conclusion are summarized in the final section.

## 2. DATA REDUCTION AND GC CANDIDATE SELECTION

### 2.1. Data

We use Wide Field Camera 3 (WFC3)/UVIS F814W( $I_{814}$ ) and WFC3/IR F160W( $H_{160}$ ) images of the target galaxies from the HST archive (PI: van den Bosch, PID: 13050/13416). Basic information of the images are listed in Table 2. For each galaxy, the total exposure times are  $\approx 500$  s for F814W and  $\approx 1400$  s for F160W. F814W images cover a field of view of  $2'.7 \times 2'.7$ , which is larger than the field of view of F160W images,  $2'.27 \times 2'.05$ . We use only F160W fields which are spatially overlapped with F814W fields for the following analysis.

For reference, we analyze Advanced Camera for Surveys (ACS)/Wide Field Channel (WFC) F475W( $g_{475}$ ), F814W( $I_{814}$ ) and WFC3/IR F160W( $H_{160}$ ) archival images

**Table 2.** HST Data for the Target MCEGs and Reference Galaxies

Galaxy	T(F475W)	T(F814W)	T(F160W)	PID
	[s]	[s]	[s]	
UGC 3816	-	696	1500	13050
NGC 0384	-	482	1350	13050
NGC 1281	-	495	1350	13050
NGC 1270	-	495	1350	13050
PGC 70520	-	489	1350	13050
NGC 0472	-	482	1350	13050
NGC 2767	-	635	1500	13050
NGC 1271	-	495	1350	13050
UGC 2698	-	805	1350	13416
MRK 1216	-	500	1350	13050
PGC 11179	-	495	1350	13050
PGC 32873	-	538	1500	13050
NGC 1399	680	1224	1197	10911, 11712
NGC 4874	5071	10425	10791	10861, 11711

of two local massive ETGs, NGC 1399 and NGC 4874. More details of these images are explained in [Blakeslee et al. \(2012\)](#) and [Cho et al. \(2016\)](#).

### 2.2. Data Reduction

We reduce the HST images following the procedures we applied in our previous studies of GCs in nearby galaxies (e.g. [Lee & Jang 2016a](#); [Lee, Jang, & Kang 2019](#)). We download individual frame images of each galaxy (`_flt` for WFC3/IR and `_flc` for the rest) from the MAST archive<sup>1</sup>. They are aligned and combined within the same filter using `DrizzlePac` ([Gonzaga et al. 2012](#)). The image scale of the combined image is  $0''.04 \text{ pixel}^{-1}$  for WFC3/UVIS F814W,  $0''.05 \text{ pixel}^{-1}$  for ACS/WFC F475W and F814W, and  $0''.10 \text{ pixel}^{-1}$  for WFC3/IR F160W. We adopt `final_pixfrac=0.8` and `final_pixscale=0.10` for WFC3/IR F160W following the values used for drizzling NGC 1399 and NGC 4874 images ([Blakeslee et al. 2012](#); [Cho et al. 2016](#)). FWHM values of the point sources are around 2 pixels for every image. Figure 1 displays pseudo-color maps of our 12 target MCEGs. Similar maps of the F160W images of 16 compact elliptical galaxies including our target galaxies are given in Figure 1 of [Yildirim et al. \(2017\)](#).

For better detection of GC candidates from the images, we detect sources after subtracting the contribution of the diffuse galaxy light from the original images. We produce a smooth, filtered image from the drizzled image of each galaxy using

a ring median filter with `IRAF/RMEDIAN` ([Secker 1995](#)). Then we subtract the smooth image from the drizzled image to produce a galaxy-light-subtracted image, and use the resulting image for source detection. We use the ring median filters with inner radius of 16 pixels and outer radius of 18 pixels. If the radius of the ring median filter is too small, then the flux of the GC candidates could be underestimated. If the radius is too large, then the galaxy light is not fully filtered. Considering these, we set the inner filter radius as 8 times the FWHM value.

We run `Source Extractor` to detect the sources in the galaxy-light-subtracted images with  $2\sigma$  threshold ([Bertin & Arnouts 1996](#)). We set `BACK_SIZE = 32` pixels and `BACKPHOTO_TYPE = LOCAL` for better detection of GC candidates near bright sources. Other settings are not changed from the default. To remove the spurious sources, we detect sources separately for the F814W and F160W images and only select sources that appear in both images with a matching tolerance of  $0''.2$ . For the selected sources, we obtain auto magnitudes and aperture magnitudes with various aperture radii ranging from 3 to 5 pixels. To get total magnitudes and colors, we correct the small aperture magnitudes by applying aperture correction as described in Section 2.4.

We adopt AB magnitudes to be consistent with previous studies of the reference galaxies NGC 1399 and NGC 4874 ([Blakeslee et al. 2012](#); [Cho et al. 2016](#)). Calibration of the instrumental magnitudes are done using the zeropoints from the online WFC3 table<sup>2</sup> or from the online ACS Zeropoint Calculator<sup>3</sup>. For the case of MCEGs, WFC3/UVIS F814W zeropoints for an infinite aperture is 25.125 (average of UVIS1 25.139 and UVIS2 25.110). ACS F475W/F814W zeropoints for an infinite aperture are 26.055 and 25.939 for NGC 1399, and 26.057 (average of 26.054 and 26.060) and 25.949 for NGC 4874. WFC3/IR F160W zeropoint for an infinite aperture is 25.946 for all cases.

### 2.3. Selection of GC Candidates

It is expected that GCs in the target galaxies appear as point-like sources or slightly resolved sources in the F814W/F160W images ([Harris 2009](#); [Lee & Jang 2016a](#); [Lee, Jang, & Kang 2019](#)). Therefore, we first select compact sources from the catalog of the detected sources using two `Source Extractor` output parameters, effective radius (`FLUX_RADIUS`) and FWHM (`FWHM_IMAGE`) as well as magnitude concentration parameter ( $C$ ). The magnitude concentration parameter used in this study is derived from the difference between two different aperture magnitudes with aperture radii of 3 pixel and 5 pixel in F814W images:  $C_{3-5} = F814W(r = 3\text{pix}) - F814W(r = 5\text{pix})$ . To set the

<sup>1</sup> <http://archive.stsci.edu/hst/>

<sup>2</sup> <https://www.stsci.edu/hst/instrumentation/wfc3/data-analysis/photometric-calibration/>

<sup>3</sup> <https://acszeropoints.stsci.edu/>



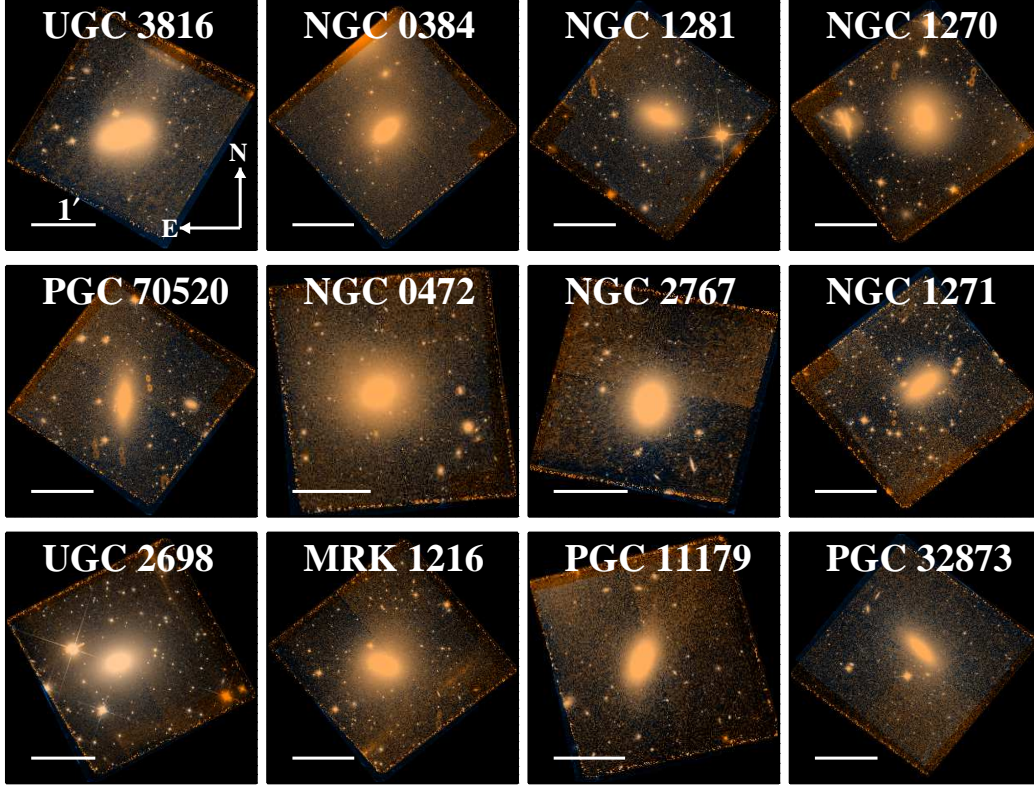


**Figure 1.** Pseudo-color stamp maps of the 12 target MCEGs. WFC3/UVIS F814W images and WFC3/IR F160W images are combined. North is up and east to the left. One arcminute scale bars are marked on the bottom left side.

parameter range for selecting compact sources, we stack the photometric results of our target MCEGs as shown in Figure 2.

In the left panel of Figure 2, we display the values of effective radius, FWHM, and concentration parameter versus F814W auto magnitude of the sources detected in our 12 MCEG images. Note that the bright narrow sequences at  $\text{FLUX\_RADIUS} \approx 1.5$  pixels,  $\text{FWHM\_IMAGE} \approx 2.0$  pixels, and  $C_{3-5} \approx 0.2$  appear in each plot, showing that they are point sources. These point sources are mostly foreground stars. Moreover, these sources show color-magnitude relations similar to the foreground stars as well (see Figures 8 to 13). However, these sequences become unclear as the magnitudes become fainter, especially in the magnitude range where GC candidates are mostly located. Therefore, we select GC candidates including these narrow sequences and then subtract the foreground contamination later as described in Section 3.4. We adopt the conditions for GC candidate selection in F814W images:  $18.0 < \text{MAG\_AUTO} < 26.0$ ,  $1.0 < \text{FLUX\_RADIUS} < 4.0$ ,  $1.5 < \text{FWHM\_IMAGE} < 5.0$ , and  $0.0 < C_{3-5} < 0.5$ . The bright limit is set considering the magnitude of the brightest GCs and the faint limit is set considering the magnitude limit. The magnitude range is initially broadly set and will be narrowed later. The ranges for the other three size parameters are very similar to those from

Blakeslee et al. (2012); Cho et al. (2016); Lee et al. (2018). We also consider flags to remove any saturated sources or sources near the image boundary and ellipticity to remove any elongated sources:  $\text{FLAGS} < 4$ ,  $\text{ELLIPTICITY} < 0.56$  for both filters. We decide to use the cut at 0.56 where a discontinuity in the ellipticity distribution of compact sources is seen.

To estimate the contamination by background sources, we display the results of the sources detected in the Hubble eXtreme Deep Field (XDF) images in the right panel of Figure 2. We use ACS/WFC F814W data with an image scale of  $0''.03 \text{ pixel}^{-1}$  and WFC3/IR F160W data with an image scale of  $0''.06 \text{ pixel}^{-1}$  provided by XDF Data Release 1.0 (Illingworth et al. 2013). Considering the image scale difference between our MCEG data and the XDF data, we convert  $\text{FLUX\_RADIUS}$ ,  $\text{FWHM\_IMAGE}$ , and  $C_{3-5}$  obtained from the XDF data to have the same angular scales as those of our MCEG data. Then we apply the same selection criteria for the GC candidates to calculate and subtract contamination caused by background galaxies. Most XDF sources selected with the same selection criteria for the GC candidates are foreground or background objects. To select only the background objects, we exclude the foreground objects with  $\text{FWHM} < 2.5$  pixels.

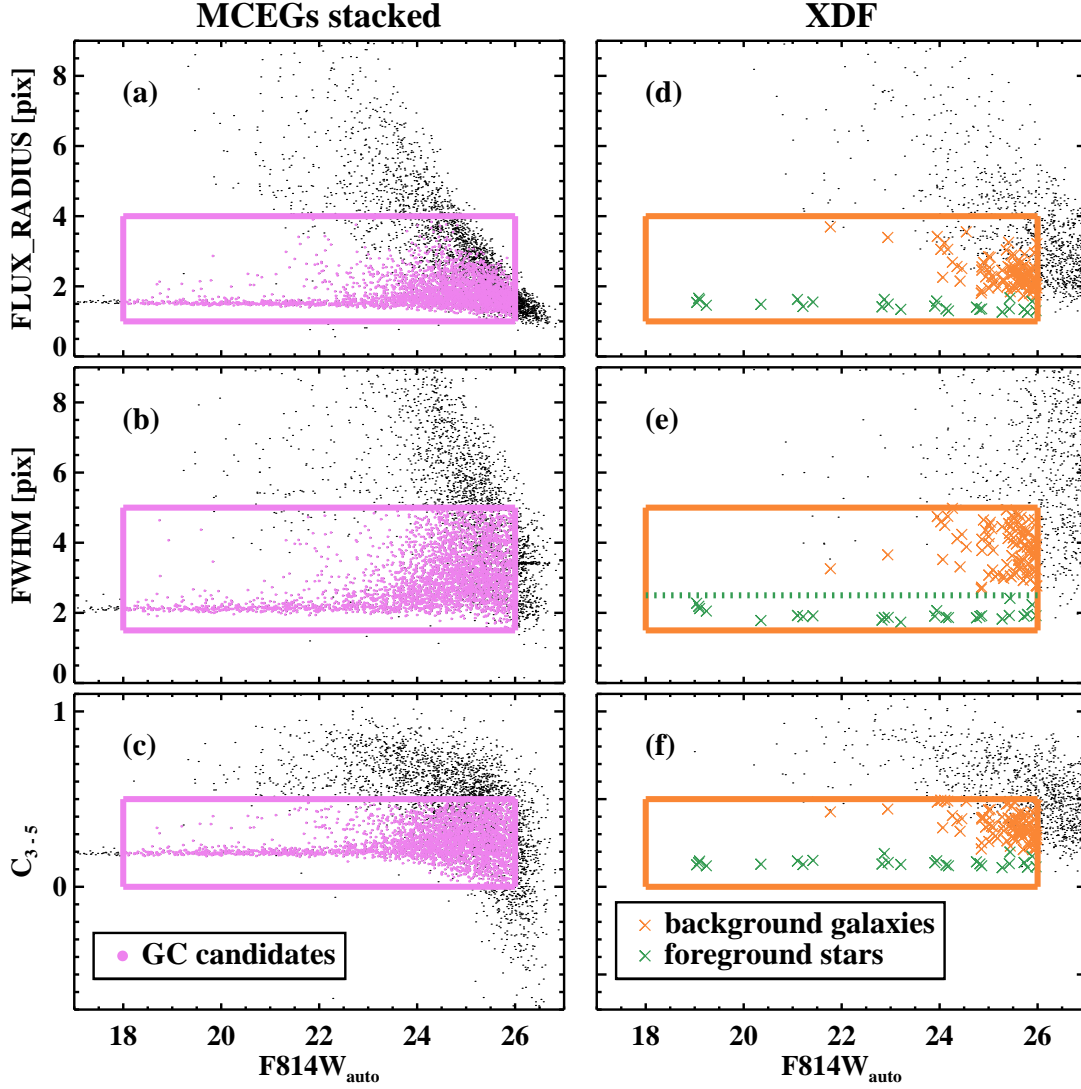


**Figure 2.** (Left panels) Effective radius (FLUX\_RADIUS), FWHM, and concentration parameter ( $C_{3-5}$ ) versus F814W auto magnitude of the sources detected in the images of the target MCEGs. We plot this diagram after stacking all the results from each MCEG. We mark the selection criteria for GC candidate in pink boxes and selected GC candidates in pink dots. We select the candidates satisfying all three size-related conditions at the same time. (Right panels) Same plots as left panels but for the sources detected in XDF images. We apply the same selection criteria as shown in orange boxes in order to calculate the background contamination. Orange crosses denote background sources and green crosses denote foreground stars with  $\text{FWHM} < 2.5$ .

For comparison, we also select GC candidates of NGC 1399 and NGC 4874 with the same selection criteria as shown in Figure 3. F814W auto magnitude range for selecting GC candidates is  $18.0 < \text{MAG\_AUTO} < 25.0$  for NGC 1399 and  $21.0 < \text{MAG\_AUTO} < 28.0$  for NGC 4874. At the distance to NGC 1399 ( $(m - M)_0 = 31.5$ ; Blakeslee et al. 2009) and NGC 4874 ( $(m - M)_0 = 35.0$ ; Carter et al. 2008), the magnitude range for the GCs ( $M_I > -13$  mag) is expected as  $\text{F814W} > 18.5$  mag for NGC 1399 and 22 mag for NGC 4874. Considering this and photometric limiting magnitudes of the data, we set the magnitude ranges to include all GC candidates with different values. Blakeslee et al. (2012) provided a catalog of their photometry for NGC 1399 GCs,

so we overlay the results and confirmed that most of the GC candidates in Blakeslee et al. (2012) are within our criteria. Cho et al. (2016) did not provide a photometric catalog for NGC 4874 GCs so we could not directly compare the results. Instead, an indirect comparison from the color-color diagram is shown in Section 3.1.

#### 2.4. Total Magnitude and Color of the GC Candidates

To derive the total magnitude and color of the GC candidates, we conduct the following procedures. First, we derive the F160W total magnitude ( $H_{160,tot}$ ) rather than the F814W total magnitude because the signal to noise ratio of the F160W images is larger than that of the F814W images.

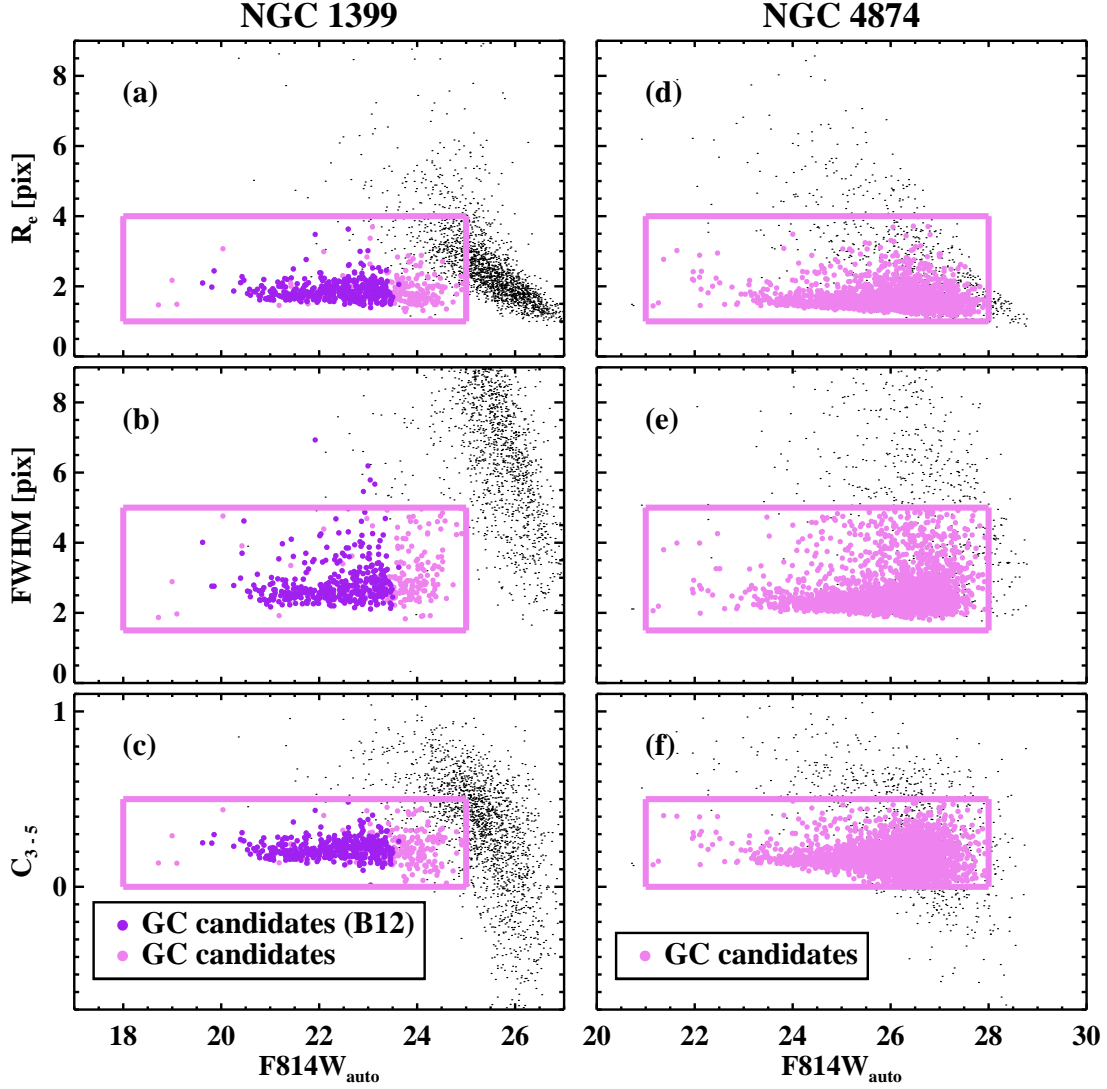


**Figure 3.** Same plots as Figure 2 but for the results of NGC 1399 (left panels) and NGC 4874 (right panels). We mark the GC candidates of each galaxy in pink dots which were selected with the same selection criteria as target MCEGs. GC candidates of NGC 1399 provided by Blakeslee et al. (2012) are marked in purple dots.

Using the value of the F160W zeropoint for an aperture with radius  $r = 0''.4$  (4 pixels), 25.755,  $H_{160,tot}$  can be derived as follows:  $H_{160,tot} = F160W(r = 4\text{pix}) - 25.946 + 25.755$ .

Second, we derive  $(I_{814} - H_{160})_{tot}$  color using the small aperture magnitudes to obtain a larger signal to noise ratio. We select the small aperture sizes considering the Point Spread Function (PSF) encircled energy fraction (EEF) from the online WFC3 table mentioned above. The PSF encircled energy fraction of the WFC3/IR F160W within the aperture radius  $r = 0''.3$  (3 pixels) is  $EEF=0.789$  which is very similar to that of WFC3/UVIS F814W within the aperture radius  $r = 0''.16$  (4 pixels),  $EEF=0.795$ . Therefore, we derive  $(I_{814} - H_{160})_{tot}$  color as follows:  $(I_{814} - H_{160})_{tot} = F814W(r = 4\text{pix}) - F160W(r = 3\text{pix}) + 2.5\log(0.795/0.789)$ . We assume that the color gradient outside the small aperture region of the GC candidates is negligible and that the encircled en-

ergy distribution of the GC candidates is similar to that of the PSF.

Finally, we derive the F814W total magnitude ( $I_{814,tot}$ ) by combining the previous results:  $I_{814,tot} = H_{160,tot} + (I_{814} - H_{160})_{tot}$ . We correct the observed magnitudes and colors for the foreground extinction using the information in Schlafly & Finkbeiner (2011), as listed in Table 1. We use ‘0’ subscripts for the foreground extinction-corrected magnitudes and colors:  $I_{814,0}$ ,  $H_{160,0}$ , and  $(I_{814} - H_{160})_0$ . We consider the internal extinction inside each of the target galaxies to be negligible, if any, because they are ETGs.

We follow the same procedures as we used for the MCEGs to derive the total magnitude and color of the GC candidates in NGC 1399 and NGC 4874. The PSF encircled energy fraction of the ACS F475W and F814W within the aperture radius  $r = 0''.15$  (3 pixels) is  $EEF=0.794$  and  $0.770$ , respec-

tively<sup>4</sup>. Therefore, we derive the colors as follows:  $(I_{814} - H_{160})_{tot} = F814W(r = 3\text{pix}) - F160W(r = 3\text{pix}) + 2.5\log(0.770/0.789)$  and  $(g_{475} - I_{814})_{tot} = F475W(r = 3\text{pix}) - F814W(r = 3\text{pix}) + 2.5\log(0.794/0.770)$ . Foreground extinction corrections are also applied.

To estimate the completeness of the GC candidate detection, we perform artificial star tests using IRAF/ARTDATA. For each galaxy, we generate 100 images with 1000 artificial point sources with FWHM = 2.0 pixels and  $(I_{814} - H_{160}) = 0.3$ , a mean color of blue GCs (see Figures 8 to 13). Similarly, we add artificial sources with  $(I_{814} - H_{160}) = 0.7$ , a mean color of red GCs to see any completeness difference between the two populations. At  $I_{814} = 25.0$  mag, the completeness is about 80% for both blue and red GC cases. The difference between the blue and red GC cases is smaller than 1% and the error for the red GC fraction due to incompleteness is estimated to be smaller than 1%.

### 3. RESULTS

Before estimating the fraction of red GCs in each MCEG, we first examine the color distributions of the GCs in NGC 1399 and NGC 4874 for references. Previous studies of extragalactic GCs based on F814W/F160W photometry are performed for only a few galaxies in the literature. To date, NGC 1399 (Blakeslee et al. 2012) and NGC 4874 (Cho et al. 2016) are the only galaxies with those colors measured so they are good references of massive ETGs for this study. NGC 1399 is a cD galaxy in the Fornax cluster with  $R_e = 10.7$  kpc and  $M_* \approx 2.6 \times 10^{11} M_\odot$  (Liu et al. 2019). NGC 4874 is a cD galaxy in the Coma cluster with  $R_e = 22.7$  kpc and  $M_* \approx 5.8 \times 10^{11} M_\odot$  (Weinzirl et al. 2014). We adopt the effective radius and the stellar mass of NGC 1399/NGC 4874 from the ACS Fornax Cluster Survey (ACS-FCS)/ACS Coma Cluster Survey (ACSCCS). The distances adopted from those surveys are 20 Mpc ( $(m - M)_0 = 31.5$ ; Blakeslee et al. 2009) for NGC 1399 and 100 Mpc ( $(m - M)_0 = 35.0$ ; Carter et al. 2008) for NGC 4874. The properties of these galaxies are also summarized in Table 1.

There are several reasons for referencing these studies for NGC 1399 and NGC 4874. First, they use the same F814W( $I_{814}$ )/F160W( $H_{160}$ ) filter systems as our study of MCEGs. This serves as useful references to compare GC systems between MCEGs and massive ETGs. We can set the selection criteria for GCs in  $(I_{814} - H_{160})$  colors. Second, they additionally use the F475W( $g_{475}$ ) filter system. We can set the criteria for dividing blue and red GC subpopulations in  $(g_{475} - I_{814})$  colors. Third, the distances to our MCEGs are in between the distances to NGC 1399 and NGC 4874. Therefore, the selection criteria for GCs and the color divi-

sion criteria determined from NGC 1399 and NGC 4874 can be similarly applied to the MCEGs.

The most important reason we need these references is that  $(I_{814} - H_{160})$  colors are not effective to divide GC samples into two separate subpopulations. Blakeslee et al. (2012) presented  $(g_{475} - I_{814})$ ,  $(g_{475} - z_{850})$  and  $(I_{814} - H_{160})$  colors of the GCs in NGC 1399, and showed that the bimodality is clearly seen in both  $(g_{475} - I_{814})$  and  $(g_{475} - z_{850})$  color distributions while it is less clear in the  $(I_{814} - H_{160})$  color distribution. Cho et al. (2016) presented similar results for NGC 4874.

Unlike  $(I_{814} - H_{160})$  colors,  $(g_{475} - I_{814})$  colors are effective to divide GCs into two subpopulations. Mixture modelling algorithms such as KMM (Ashman et al. 1994) or Gaussian Mixture Modeling (GMM; Muratov & Gnedin 2010) is often applied to optical color distributions to derive the fractions of blue and red subpopulations (e.g. Peng et al. 2006; Blakeslee et al. 2012; Lee, Jang, & Kang 2019). Therefore, from  $g_{475}$ ,  $I_{814}$ ,  $H_{160}$  photometric studies of GCs in NGC 1399 and NGC 4874, we first determine a  $(g_{475} - I_{814})$  color criterion for dividing blue and red subpopulations. Then we determine a corresponding  $(I_{814} - H_{160})$  color criterion from the relations between those two colors derived in this study. More details are explained in the next section. We use this fixed  $(I_{814} - H_{160})$  color criterion to estimate the GC fractions of each MCEG. Using cD galaxies as a reference does not bias the color-color relation because the intrinsic properties of GC subpopulations (age, metallicity, etc.) are similar in every massive galaxy (Brodie & Strader 2006).

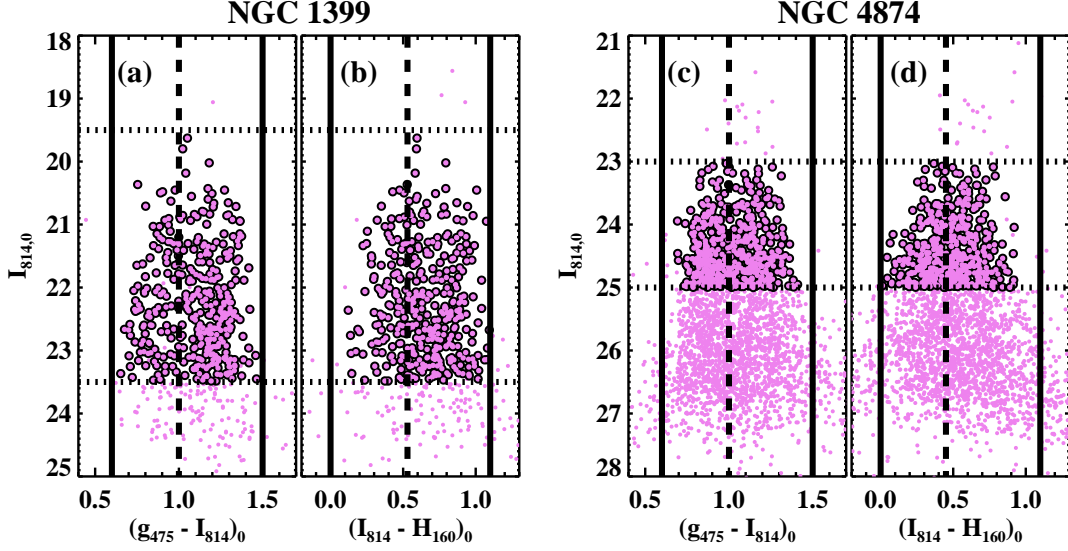
#### 3.1. Color Distributions of the GCs in NGC 1399 and NGC 4874

Figure 4 shows  $I_{814,0}$  vs.  $(g_{475} - I_{814})_0$  and  $I_{814,0}$  vs.  $(I_{814} - H_{160})_0$  CMDs of the GC candidates in NGC 1399 and NGC 4874 selected in the previous section. Note that most of the GC candidates selected through size information exhibit GC-like colors, meaning that they are indeed GC candidates. We set the color range to select GCs in each galaxy to be  $0.6 < (g_{475} - I_{814})_0 < 1.5$  and  $0.0 < (I_{814} - H_{160})_0 < 1.1$  based on the bright GC candidates in NGC 1399 ( $19.5 < I_{814,0} < 23.5$  mag) and NGC 4874 ( $23.0 < I_{814,0} < 25.0$  mag). The magnitude ranges of the bright GC candidates are adopted from the previous studies of each galaxy which were used to derive the color-color relation. We follow those magnitude ranges for the bright GCs hereafter.

Figures 5(a) and (b) shows  $(I_{814} - H_{160})_0$  vs.  $(g_{475} - I_{814})_0$  color-color diagrams of the bright GCs in NGC 1399 and NGC 4874. We overlay linear color-color relations derived in this study after  $3\sigma$  clipping iteratively (red dashed lines):  $(I_{814} - H_{160})_0 = (1.14 \pm 0.03)(g_{475} - I_{814})_0 - (0.61 \pm 0.04)$  with an RMS value of 0.13 for NGC 1399 and

<sup>4</sup> <https://www.stsci.edu/hst/instrumentation/acs/data-analysis/aperture-corrections>





**Figure 4.** CMDs of the GC candidates in (a,b) NGC 1399 and (c,d) NGC 4874. All the GC candidates marked in Figure 3 are also marked in pink dots. The bright GC candidates in NGC 1399 ( $19.5 < I_{814,0} < 23.5$ ) and NGC 4874 ( $23.0 < I_{814,0} < 25.0$ ) are marked in black circles, and the corresponding magnitude ranges are marked in dotted lines. The solid lines denote the color range for selecting the GCs and the dashed lines denote the color used for dividing blue and red GC population.

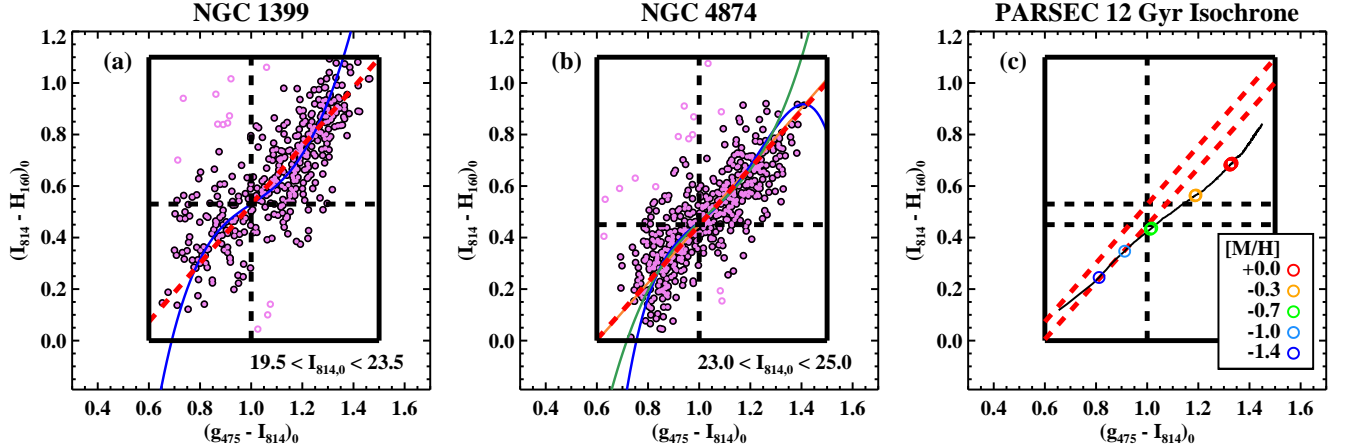


**Figure 5.** Color-color diagrams of the bright GC candidates in (a) NGC 1399 and (b) NGC 4874. The blue line in (a) is a quartic relation for NGC 1399 GCs given by Blakeslee et al. (2012) shifted by  $-0.04$  in y-axis. The orange, green, and blue lines in (b) are linear, cubic, and quartic relations for NGC 4874 GCs given by Cho et al. (2016). The red dashed lines in (a,b) are linear relations derived in this study for each galaxy after  $3\sigma$  clipping. The clipped sources are marked in open pink circles, and filled pink circles are sources used to derive the relation. (c) Color-color relation derived from PARSEC 12 Gyr isochrone. We mark  $[M/H]$  values along with the relation. The same red dashed lines in (a,b) are also marked for comparison. In all the three diagrams, the black solid lines denote the color range for selecting the GCs and the dashed lines denote the color used for dividing blue and red GC populations.

$(I_{814} - H_{160})_0 = (1.11 \pm 0.03)(g_{475} - I_{814})_0 - (0.66 \pm 0.03)$  with an RMS value of 0.11 for NGC 4874. If we change the faint magnitude limit to include fainter GCs, the scatter of the relation increases but the overall relation changes little. The color-color relations suggested by Blakeslee et al. (2012) (eq. 1) and Cho et al. (2016) (eqs. 9 to 11) are also overlaid. In the case of NGC 4874, the bright GCs follow the relations very well and the linear relation of the GCs in this study shows a tight correlation with the relations of Cho et al. (2016). This means that the photometric results de-

rived in this study agree well with the previous study. However, in the case of NGC 1399, there is a slight disagreement between our relation and the previously derived relation. This difference arises because Blakeslee et al. (2012) did not consider color corrections caused by different apertures. In Section 2.4, we correct  $(g_{475} - I_{814})$  color as much as  $2.5 \log(0.794/0.770) = 0.033$  and  $(I_{814} - H_{160})$  color as much as  $2.5 \log(0.770/0.789) = -0.026$ , which can explain the difference between our relation and Blakeslee et al. (2012)'s relation. Therefore, we mark the relation after shift-

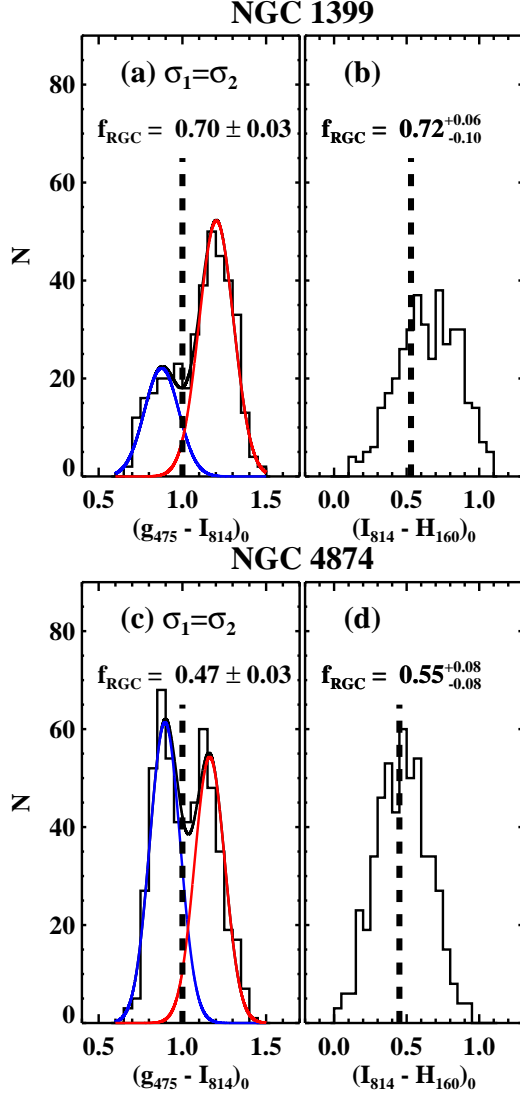


**Figure 6.** Color distributions of the bright GCs in (a,b) NGC 1399 ( $19.5 < I_{814,0} < 23.5$ ) and (c,d) NGC 4874 ( $23.0 < I_{814,0} < 25.0$ ). GMM analysis results for  $(g_{475} - I_{814})_0$  colors with an equal width option are marked in blue and red curves. The dashed lines denote the color used for dividing blue and red GC populations.

ing the relation by -0.04 in y-axis to be consistent with the fitting of this study.

Another feature is that  $(I_{814} - H_{160})_0$  colors for given  $(g_{475} - I_{814})_0$  colors of the NGC 4874 GCs are, on average, 0.1 bluer than those of the NGC 1399 GCs. This color difference also exists between the relation suggested by Blakeslee et al. (2012) and Cho et al. (2016), as already pointed out in Cho et al. (2016). This is caused mainly by the difference in the distances to the two galaxies. The distance to NGC 1399 is about five times smaller than the distance to NGC 4874 so that the light distribution of the GCs in NGC 1399 deviate from that of the PSF more than that of the GCs in NGC 4874. This difference appears mostly in

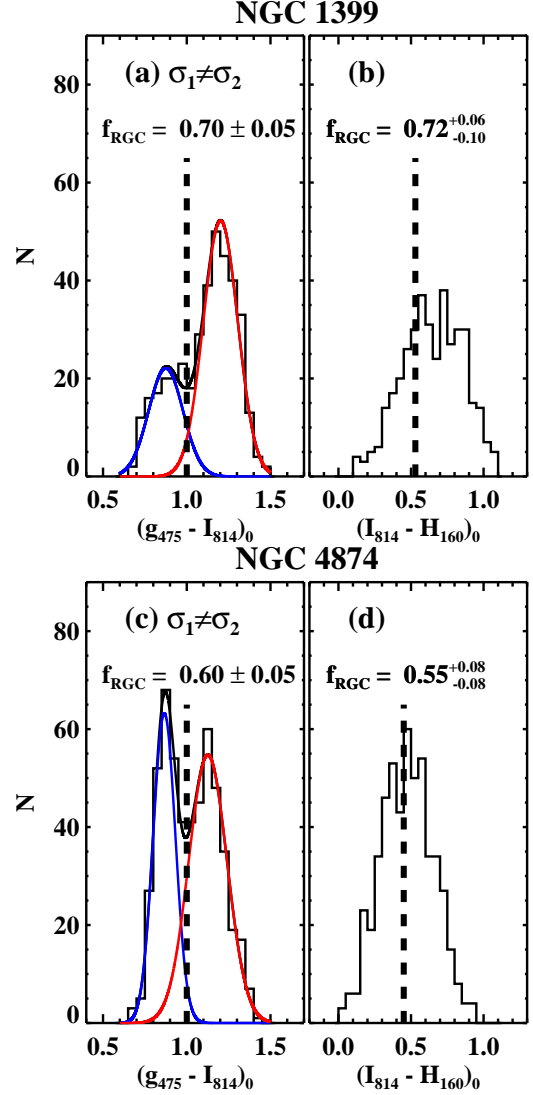


**Figure 7.** Same plot as Figure 6 but the GMM analysis results with an unequal width option are marked.

$(I_{814} - H_{160})$  color rather than in  $(g_{475} - I_{814})$  color. In this study we apply the same aperture correction to both galaxies and adopt the different color-color relation of each galaxy.

Figure 5(c) shows a color-color relation derived from Padova and TRIESTE Stellar Evolution Code (PARSEC v1.2S; Bressan et al. 2012) 12 Gyr isochrone. The simple stellar population integrated magnitudes are obtained with the default options in the web interface CMD 3.1<sup>5</sup>, e.g. Chabrier lognormal IMF. Note that the division color at  $(g_{475} - I_{814}) = 1.0$  in the model corresponds to  $(I_{814} - H_{160}) = 0.42$ , which is very similar to the case for NGC 4874 ( $(I_{814} - H_{160}) = 0.45$ ) and is 0.11 smaller than the value for NGC 1399 ( $(I_{814} - H_{160}) = 0.53$ ).

<sup>5</sup> [http://stev.oapd.inaf.it/cgi-bin/cmd\\_3.1](http://stev.oapd.inaf.it/cgi-bin/cmd_3.1)

**Table 3.** The GMM Analysis Results for the  $(g_{475} - I_{814})_0$  color distributions of the GCs in NGC 1399 and NGC 4874

Galaxy	Case	$\mu_1$	$\sigma_1$	$N_1$	$\mu_2$	$\sigma_2$	$N_2$	$f_2$	$D$	$p$	$k$
NGC 1399	$\sigma_1 = \sigma_2$	$0.88 \pm 0.01$	$0.10 \pm 0.01$	$115 \pm 11$	$1.20 \pm 0.01$	$0.10 \pm 0.01$	$268 \pm 11$	$0.70 \pm 0.03$	$3.2 \pm 0.2$	$< 10^{-3}$	-0.681
	$\sigma_1 \neq \sigma_2$	$0.88 \pm 0.03$	$0.10 \pm 0.01$	$116 \pm 19$	$1.20 \pm 0.01$	$0.10 \pm 0.01$	$267 \pm 19$	$0.70 \pm 0.05$	$3.2 \pm 0.3$	$< 10^{-3}$	-0.681
NGC 4874	$\sigma_1 = \sigma_2$	$0.90 \pm 0.01$	$0.09 \pm 0.01$	$278 \pm 14$	$1.16 \pm 0.01$	$0.09 \pm 0.01$	$245 \pm 14$	$0.47 \pm 0.03$	$3.0 \pm 0.2$	$< 10^{-3}$	-0.966
	$\sigma_1 \neq \sigma_2$	$0.87 \pm 0.01$	$0.07 \pm 0.01$	$212 \pm 24$	$1.13 \pm 0.01$	$0.11 \pm 0.01$	$311 \pm 24$	$0.60 \pm 0.05$	$2.8 \pm 0.2$	$< 10^{-3}$	-0.966

NOTE—See Figures 6 and 7.

Figures 6 and 7 show the color distributions of the bright GCs in NGC 1399 and NGC 4874. In the  $(g_{475} - I_{814})_0$  distribution of the GCs in NGC 1399, a minimum between two peaks (a dip) is found to be at  $(g_{475} - I_{814})_0 \approx 1.0$  (see also Figure 8 in Blakeslee et al. 2012). Similarly, a dip is seen clearly at  $(g_{475} - I_{814})_0 \approx 1.0$  for NGC 4874 GCs (see also Figure 13 in Cho et al. 2016). These results are very similar to the results from the previous studies.

To divide the GCs into two subpopulations statistically, we apply GMM analysis to  $(g_{475} - I_{814})_0$  distribution of the GCs (Muratov & Gnedin 2010). Figure 6 is based on the GMM analysis with an equal variance option (i.e. homoscedastic case) and Figure 7 with an unequal variance option (i.e. heteroscedastic case). The results are summarized in Table 3. According to the analysis, there is a clear bimodality in  $(g_{475} - I_{814})_0$  color for both homoscedastic and heteroscedastic cases (separation  $D > 2$ , p-value  $p < 10^{-3}$ , and kurtosis  $k < 0$ ). Moreover, the two populations are divided almost at the same color,  $(g_{475} - I_{814})_0 \approx 1.0$ , for all cases. By applying different color-color relation for each galaxy,  $(g_{475} - I_{814})_0 = 1.0$  corresponds to  $(I_{814} - H_{160})_0 = 0.53 \pm 0.05$  for NGC 1399 and  $0.45 \pm 0.04$  for NGC 4874. These values are also marked in Figures 4 and 5 and are used to divide the GCs in our target MCEGs.

### 3.2. Estimation of the Red GC Fractions of NGC 1399 and NGC 4874

We estimate the fraction of red GCs in NGC 1399 and NGC 4874 using the photometry derived in this study. In the case of  $(g_{475} - I_{814})_0$  color distributions for NGC 1399, we obtain  $f_{RGC} = 0.70 \pm 0.03$  if we apply the GMM with an equal variance option and  $0.70 \pm 0.05$  if we adopt an unequal variance option. This is consistent with the results of Blakeslee et al. (2012),  $0.68 \pm 0.04$  and  $0.71 \pm 0.03$ . In the case of  $(g_{475} - I_{814})_0$  color distributions for NGC 4874, we obtain  $f_{RGC} = 0.47 \pm 0.03$  if we apply the GMM with an equal variance option and  $0.60 \pm 0.05$  if we adopt an unequal variance option. This is also consistent with the results of Cho et al. (2016),  $f_{RGC} = 0.493 \pm 0.031$  and  $0.604 \pm 0.083$ . From  $(I_{814} - H_{160})_0$  color distributions with a fixed division color, we derive  $f_{RGC} = 0.72^{+0.06}_{-0.10}$  for NGC 1399 and

$0.55^{+0.08}_{-0.08}$  for NGC 4874. The errors for the red GC fraction are determined from the error for the division color.

The most important result from the analysis of NGC 1399 and NGC 4874 GCs is that the values of red GC fraction derived from  $(g_{475} - I_{814})_0$  and  $(I_{814} - H_{160})_0$  are very similar. This indicates that the fractions of red GCs derived from the two colors are consistent with each other. Therefore, we can safely derive the red GC fraction based on  $(I_{814} - H_{160})_0$  color for our target MCEGs. Moreover, the distances to our target MCEGs are mostly in between the distance to NGC 1399 and NGC 4874, so blue and red GCs would be divided at  $(I_{814} - H_{160})_0 = 0.45$  to  $0.53$ . In the next section, we adopt both  $(I_{814} - H_{160})_0 = 0.45$  and  $0.53$  and derive the minimum and the maximum value of the red GC fractions. The mean red GC fractions are derived using  $(I_{814} - H_{160})_0 = 0.49 \pm 0.04$ , an average value of  $0.45$  and  $0.53$ .

### 3.3. Color Distribution of the GCs in the Local MCEGs

In the left panels of Figures 8 to 13 we display the  $I_{814,0}$  vs.  $(I_{814} - H_{160})_0$  CMDs of the GC candidates for the target MCEGs. We plot the magnitudes and colors of the sources corrected for the foreground extinction to be consistent with each other. In the figure, we draw three vertical lines as guide lines at  $(I_{814} - H_{160})_0 = 0.0, 0.49$ , and  $1.1$ .  $(I_{814} - H_{160})_0 = 0.0$  and  $1.1$  are boundaries for the GC colors, and  $(I_{814} - H_{160})_0 = 0.49$  is the dividing line between blue and red GCs. This is the average of  $0.53$  and  $0.45$ , which were determined from NGC 1399 and NGC 4874. We also draw two horizontal lines at  $M_I = -13.0$  and  $I_{814,0} = 25.0$  which are boundaries for the GC magnitude cut. The absolute magnitude range for GCs is, in general,  $M_I > -13$  mag. Therefore, we set the upper magnitude limit to  $M_I = -13$  mag for GC selection considering the distance to each galaxy. To derive the color distributions of the GC candidates in the MCEGs, we choose relatively bright GCs with  $I_{814,0} < 25.0$  mag ( $M_I \approx -10.0$  to  $-8.5$  mag depending on the distances to the target galaxies) which are rarely affected by incompleteness of our photometry and have smaller photometric errors ( $err(I_{814} - H_{160}) < 0.1$ ). We exclude GC candidates brighter than  $M_I = -13.0$  mag because they are mostly foreground stars. At first, some of them were considered as ultra-

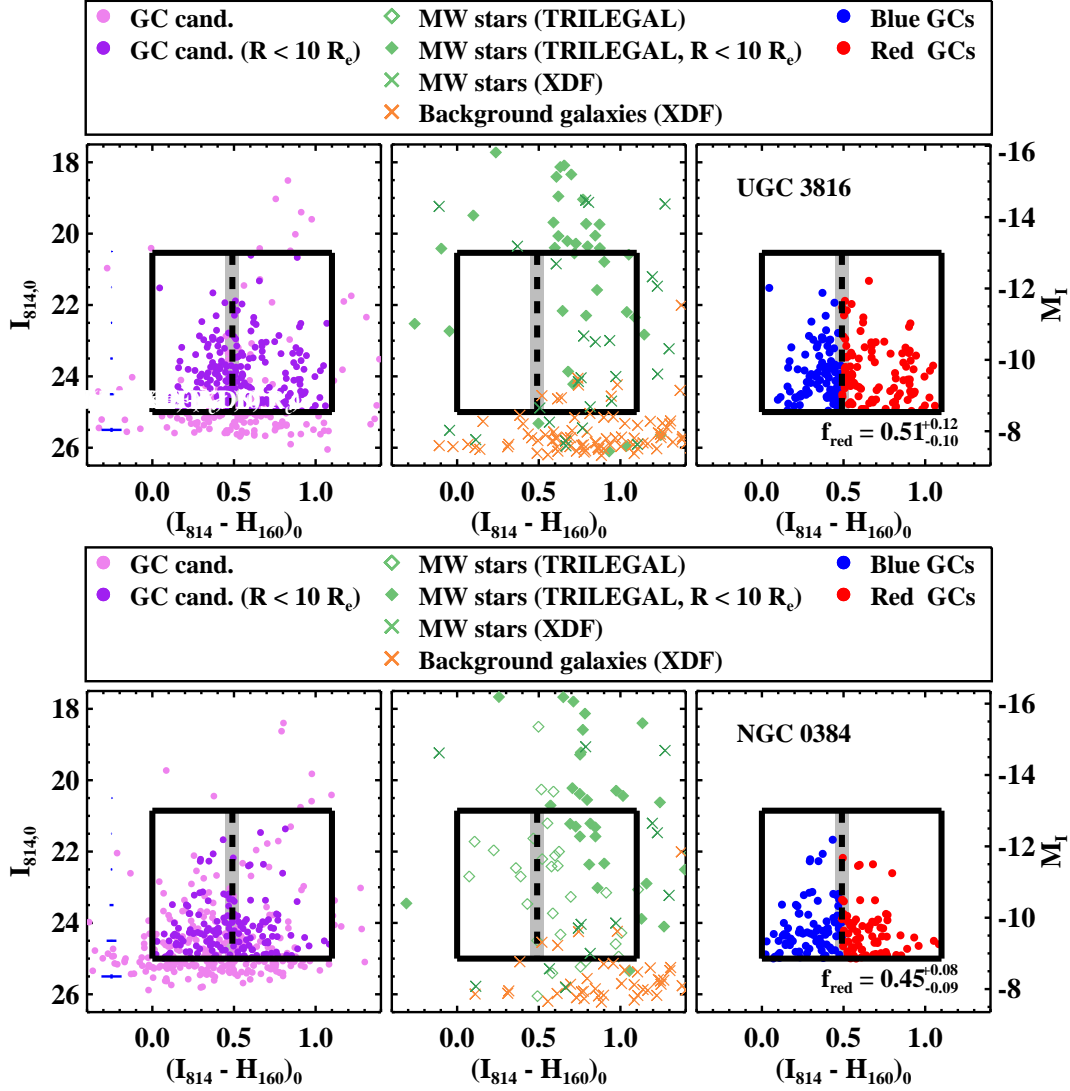


**Figure 8.** (Left) CMDs of the GC candidates of our 12 target MCEGs. All the GC candidates marked in Figure 2 are also marked in pink dots. The selected GCs with  $R < 10R_{e,circ}$  within the black boxes are marked in purple dots. The color range of the GCs is  $0.0 < (I_{814} - H_{160})_0 < 1.1$  and the magnitude range is  $M_I > -13.0$  and  $I_{814,0} < 25.0$ . Blue errorbars in the left denote mean photometric errors for given magnitude bins. (Middle) CMDs of the MW stars generated by TRILEGAL model (green diamonds) and foreground/background sources found in XDF (green and orange crosses). (Right) CMDs of the GC candidates after removing foreground stars with  $R < 10R_{e,circ}$  statistically. We mark blue and red GCs according to the color division  $(I_{814} - H_{160})_0 = 0.49 \pm 0.04$  as marked in dashed lines, and mark the red GC fractions.

compact dwarfs (UCDs), but the possibility was ruled out after comparing CMDs with model CMDs of foreground stars, as will be shown in the next section. We also choose GCs inside the circular region of the host galaxy ( $R < 10R_{e,circ}$ ) to minimize contamination from background sources and other nearby galaxies. The boundary at  $R = 10R_{e,circ}$  is large enough to select most of the GCs belonging to our target galaxies, and Beasley et al. (2018) also used the same boundary at  $R = 10R_{e,circ}$  to estimate the red GC fraction of NGC 1277.

The most distinguishable feature in the CMDs is that the target MCEGs host a rich population of sources with  $0.0 < (I_{814} - H_{160})_0 < 1.1$ , a similar color range for the GCs in

NGC 1399 and NGC 4874, implying that the selected GC candidates with this color range in the target MCEGs are mostly genuine GCs. They are indeed GCs similar to those in NGC 1399 or NGC 4874.

### 3.4. Estimation of the Red GC Fractions of the Local MCEGs

Before estimating the red GC fractions of each galaxy, we check foreground star contamination using the TRILEGAL MW model for each galaxy (Girardi et al. 2005)<sup>6</sup>. We

<sup>6</sup> <http://stev.oapd.inaf.it/cgi-bin/trilegal>



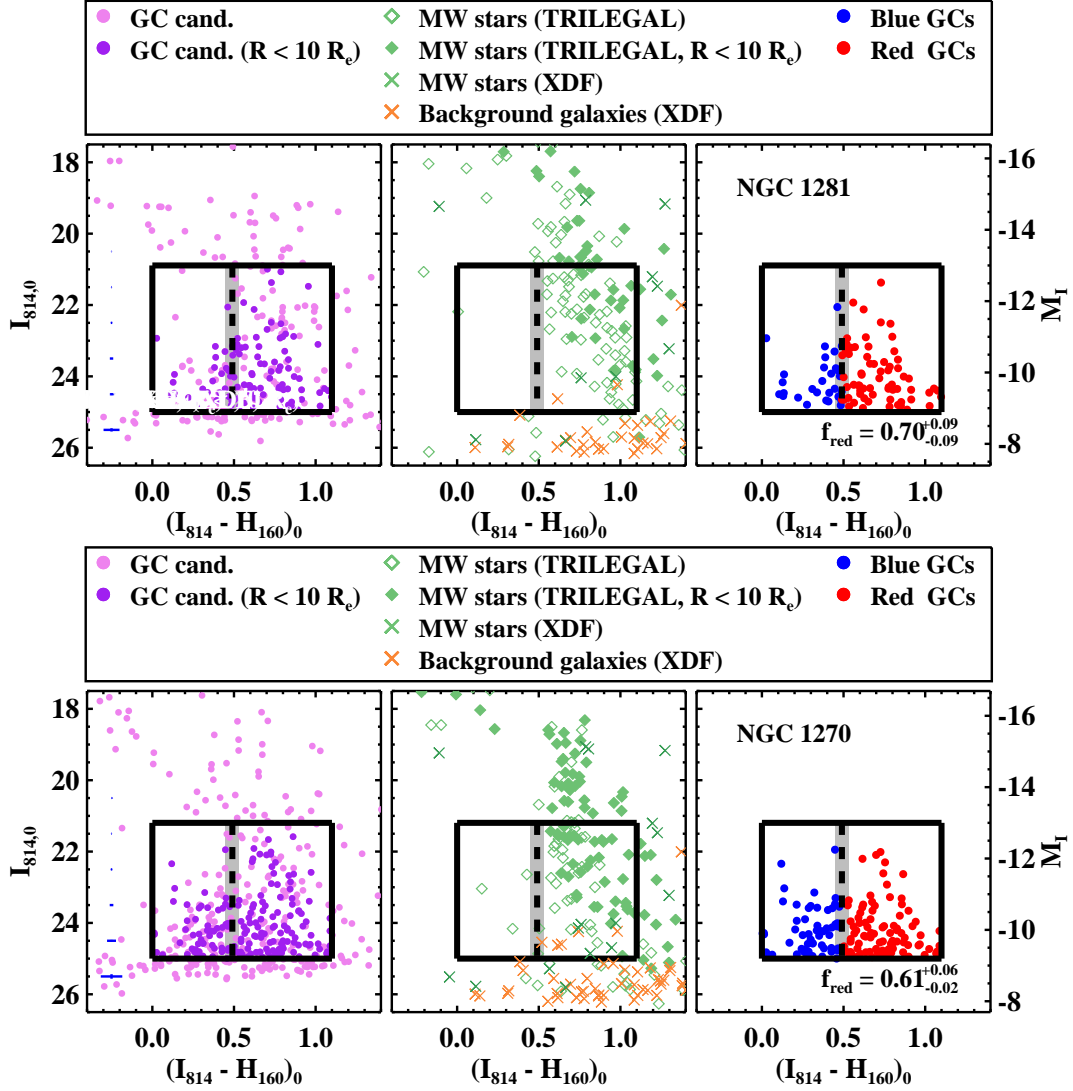


Figure 9. Figure 8 continued.

generate model stars according to the galactic coordinate of each galaxy and the field area. The area is restricted to  $R < 10R_{e,circ}$  for each galaxy similar to the area used to select GCs. We plot the CMD derived from the model in the middle panels of Figures 8 to 13 in green diamonds. Open symbols represent model stars within the HST field and filled symbols represent those within  $R < 10R_{e,circ}$  for each galaxy. Clearly, the galaxies located in low galactic latitude show a large number of model stars (NGC 1281, NGC 1270, NGC 1271, UGC 2698) and most of the red sources show a color distribution similar to that of model foreground stars. Therefore, we exclude model stars statistically from our CMDs to estimate the red GC fraction properly. We divide the CMD region with a magnitude bin of 0.5 and a color bin of 0.1 and then subtract the number of MW model stars from the number of GC candidates. The final CMDs are shown in the right panels of Figures 8 to 13.

We also check background galaxy contamination from the HST image. The field of view of our images is not large enough to estimate the background contribution, so we use the XDF field as a background field (Illingworth et al. 2013). The target galaxies are located in various locations in the sky so the XDF may not necessarily represent a background for each target galaxy. However, it is still useful to estimate the background contamination level. We apply the same photometric procedures as used for our target galaxies to the XDF F814W/F160W images and derive  $(I_{814} - H_{160})_0$  distribution of the point sources. As a result, we find fewer than seven GC-like background sources with  $I_{814,0} < 25.0$  mag and  $R < 10R_{e,circ}$ , which negligibly affect the estimation of the red GC fraction. They are marked in orange crosses in Figures 8 to 13. Therefore, we do not correct for the background galaxy contamination.

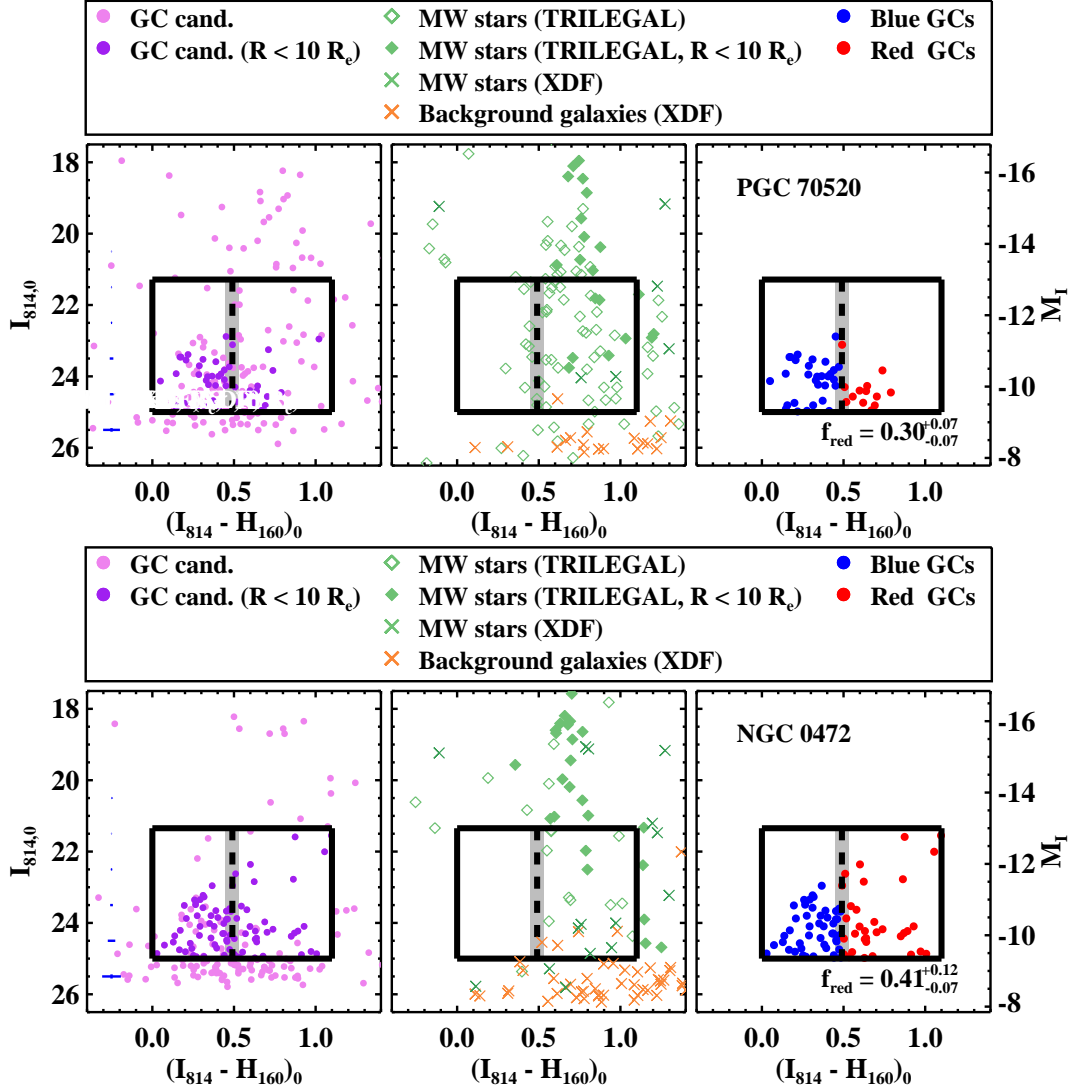


Figure 10. Figure 8 continued.

In Table 4 we summarize the number of GC candidates before and after contamination correction, and the number of contaminants for each galaxy. The fractions of foreground contaminants range from 0 to 24% (mostly smaller than 10%), and those of background contaminants are less than 6%. Thus, the effect of background contaminants is not impacting the results discussed in this study.

Now we are ready to estimate the red GC fraction of the target MCEGs. From the final CMDs, we divide the GCs in each of our target MCEGs into blue and red subpopulations using  $(I_{814} - H_{160})_0 = 0.49$  as a division criterion: blue GCs with  $0.0 < (I_{814} - H_{160})_0 < 0.49$  and red GCs with  $0.49 \leq (I_{814} - H_{160})_0 < 1.1$ . Then we calculate the fraction of red GCs in the entire sample of GCs with  $I_{814,0} < 25.0$  mag in each galaxy. Similarly, we calculate the minimum and the maximum value of the fraction of red GCs using  $(I_{814} - H_{160})_0 = 0.53$  and  $0.45$ , respectively. The results are shown

in the right panels of Figures 8 to 13 and are summarized in Table 1. The fractions of red GCs in our target MCEGs range from  $f_{RGC} = 0.2$  to  $0.7$ , and NGC 1281 shows the highest red GC fraction,  $f_{RGC} = 0.70 \pm 0.09$ .

### 3.5. Spatial and Radial Distributions of the GCs in the Local MCEGs

In Figure 14 we show the spatial distribution of the blue and red GCs in each of the target MCEGs. The GCs in each of the MCEGs show a central concentration, which implies that most of the GCs we select are indeed the members of each galaxy. We restrict the spatial range for selecting GCs at  $R < 10R_{e,circ}$ , similar to the value used for NGC 1277 in Beasley et al. (2018), to compare the red GC fraction equivalently.

We also show the spatial distribution of the GCs in the two reference galaxies. Because they are much larger than the MCEGs, only the central region is covered by the HST im-

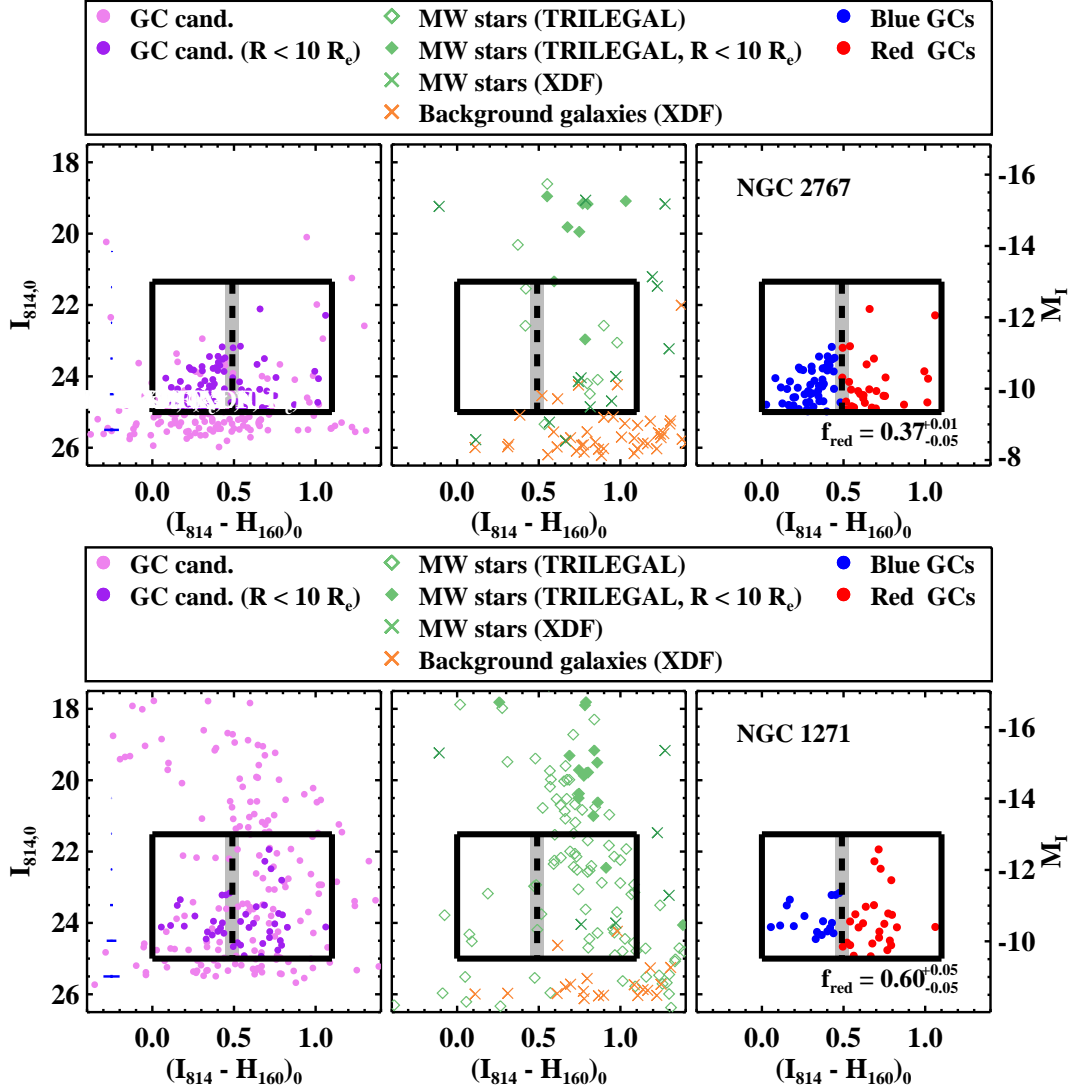


Figure 11. Figure 8 continued.

ages so it is hard to see a central concentration clearly. In the figure, large solid circles around the two reference galaxies denote  $R = 0.5R_e$  while large dashed circles around the target MCEGs denote  $R = 10R_e$ .

In Figure 15 we show the radial number density profiles of all GCs as well as blue and red subpopulations. The very central regions of the MCEGs are incomplete so we mask the inner regions at  $R < 2''.5$  when deriving the radial profile for each MCEG. In general, the radial number density of the GCs in the MCEGs decreases as the projected galactocentric distance increases, and this indicates that most of the GCs we selected are indeed the members of each galaxy. All the fields cover  $R > 10R_{e,circ}$  so the coverage is expected to be wide enough to select most of the GCs belonging to the galaxies. However, most of the profiles decrease continuously because they are not wide enough to measure the stable background number density.

We also show the radial distribution of the GCs in the two reference galaxies. In general we can see the difference between red GC profile and blue GC profile in giant ETGs, but it is not shown here because these two galaxies are not fully covered by the HST images.

#### 4. DISCUSSION

##### 4.1. Mass-Size Relations of the Local MCEGs in Comparison with the Virgo, Fornax, and Coma ETGs

In Figure 16(a) we display effective radii ( $R_e$ ) vs. stellar masses ( $M_*$ ) of our target MCEGs in comparison with the Virgo ETGs in the ACS Virgo Cluster Survey (ACSVCS; Ferrarese et al. 2006; Peng et al. 2008), the Fornax ETGs in the ACSFCS (Liu et al. 2019), and the Coma ETGs in the ACS CCS (Weinzirl et al. 2014). We also plot the empirical mass-size relation for  $z = 0 - 3$  given by van der Wel et al. (2014) for comparison. To compare the stellar mass properly,

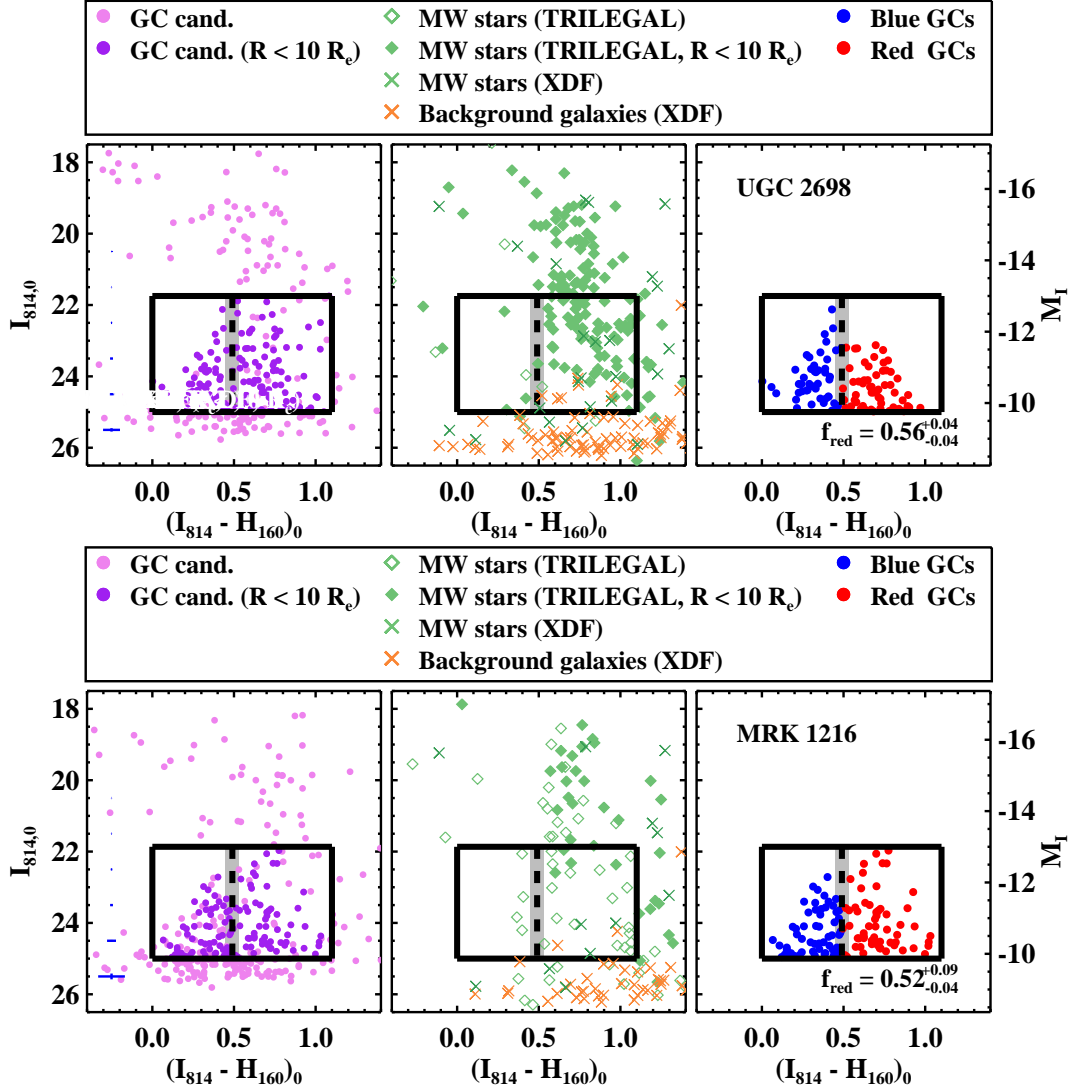


Figure 12. Figure 8 continued.

we consider the mass-to-light ratio (M/L) difference among adopted IMFs:  $M/L$  (Salpeter) = 1.6  $M/L$  (Kroupa) = 1.8  $M/L$  (Chabrier). Therefore, we increase the stellar masses of ACSVCS ETGs and mass-size relation by 1.8 where the Chabrier IMF was adopted. We also increase the stellar masses of ACSVCS ETGs by 1.6 where the Kroupa IMF was adopted.

Distinguishable features in this figure are as follows. First, all the ETGs in Virgo, Fornax, and Coma follow a well-known mass-size relation in the sense that the effective radii of the ETGs increase as their stellar masses increase. In Virgo and Fornax, most galaxies with low stellar mass (i.e.  $M_* < 10^{11} M_\odot$ ) have smaller effective radii of  $R_e < 3$  kpc, while those with high stellar mass (i.e.  $M_* > 10^{11} M_\odot$ ) have much larger effective radii of  $R_e > 7$  kpc. The ETGs in Coma follow a similar trend to that of Virgo or Fornax: most galaxies with low stellar mass have smaller effective radii of

$R_e < 5$  kpc, while those with high stellar mass have much larger effective radii of  $R_e > 17$  kpc.

Second, there is an empty region at  $M_* > 10^{11} M_\odot$  and  $R_e < 7$  kpc where almost no Virgo, Fornax, or Coma ETGs are found. This shows that there are almost no MCEGs in such clusters. The MCEGs in our sample occupy the above empty region. NGC 1277 is also included in the same region. The MCEGs also follow a similar trend in the mass-size relation, but with a significant offset in effective radii from those of the massive ETGs: they are much smaller than the massive ETGs with similar stellar mass. The mass-size relation of the MCEGs is consistent with the relation for  $z \approx 2$  given by [van der Wel et al. \(2014\)](#), as noted in [Yildırım et al. \(2017\)](#).

In summary, the MCEGs in our sample might have evolved via different routes compared with the massive ETGs in Virgo, Fornax, or Coma: the former might have grown much less in size than the latter since their formation. It may be



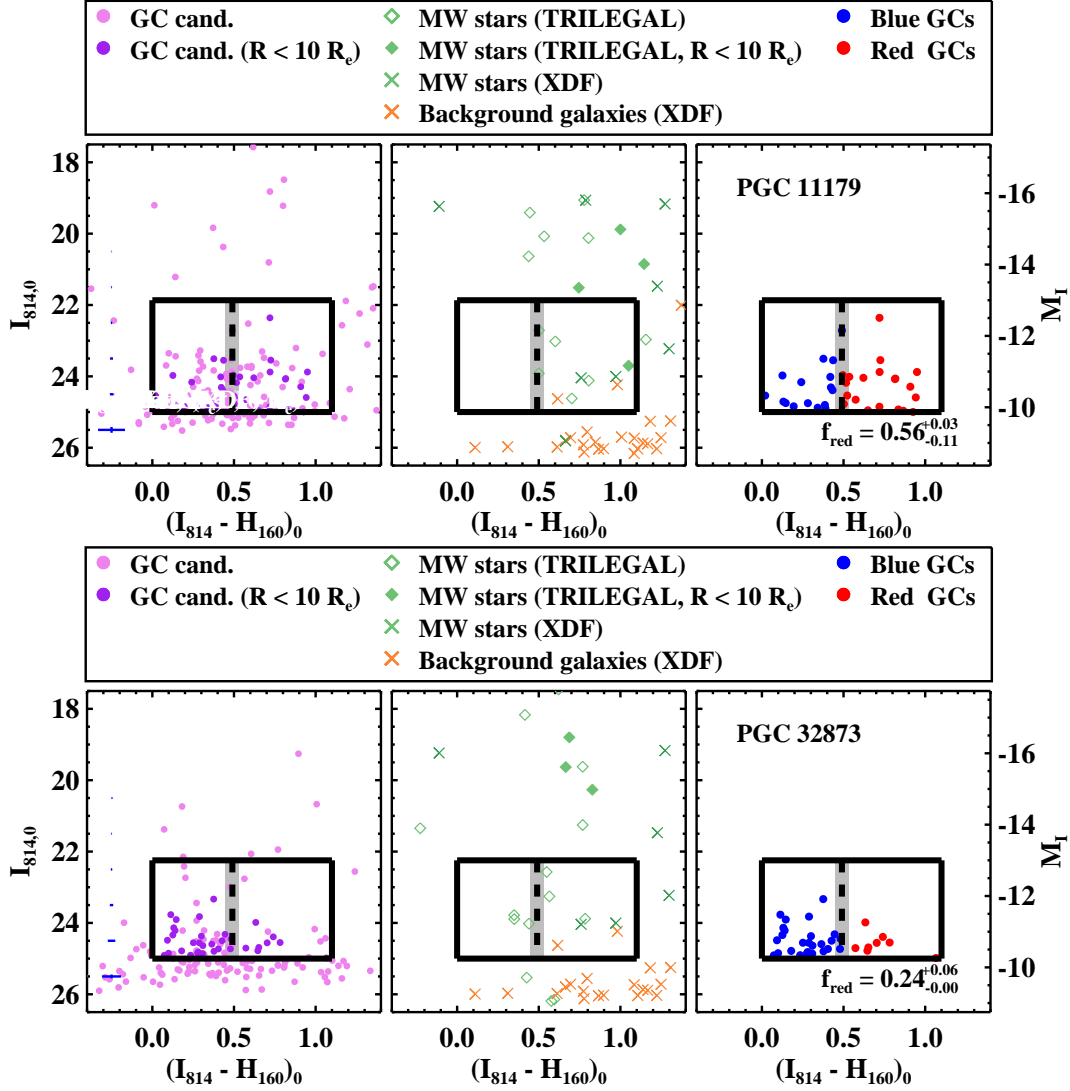


Figure 13. Figure 8 continued.

possible that they follow the different mass-size relation because our sample of MCEGs are located in less dense environments than the cluster ETGs we have compared. However, about half of our sample of MCEGs are also located in cluster environment: NGC 1270, NGC 1271, NGC 1281, and UGC 2698 are members of the Perseus cluster (Abell 426) with NGC 1277, and PGC 11179 is a member of Abell 400. We will further discuss the environment of our sample of MCEGs in the next section.

In Figure 16(b) we display central velocity dispersion ( $\log \sigma_c$ ) vs. stellar mass ( $M_*$ ) of our target MCEGs, NGC 1277, and the two reference galaxies. We also plot the empirical mass-velocity dispersion relation for  $z = 0 - 2$  given by Cannarozzo et al. (2020) for comparison. Here we increase the stellar mass of mass-dispersion relation by 1.8 where the Chabrier IMF was adopted. The relation of the MCEGs is consistent with the relation for  $z \approx 2$ .

Thus, the MCEGs follow the mass-size relation and mass-velocity dispersion relation for galaxies at  $z \approx 2$ . This supports that the MCEGs in this study are strong candidates for relic galaxies.

#### 4.2. Red GC Fractions vs. Galaxy Properties

For the comparison of red GC fractions in our sample of MCEGs, we use the results for the Virgo ETGs in the ACSVCS sample (Peng et al. 2008). They are based on the analysis of the HST/ACS data for a large number of galaxies. For the calculation of the fractions of blue and red GCs in each galaxy of the ACSVCS sample, Peng et al. (2008) applied a hybrid approach to divide the GC sample of a galaxy into a blue subpopulation and a red subpopulation. For the case of the brightest 21 galaxies (with  $M_B < -19.1$  mag) they used a dip between the two Gaussians in the KMM two-Gaussian fits for the  $(g_{475} - z_{850})$  distribution of the GCs. They adopted a homoscedastic option in the KMM

**Table 4.** Number of GC Candidates and Contaminants

Galaxy	N(GC cand.)	N(foreground)	N(background)	f(foreground)	f(background)	N(final GCs)
	[A]	[B]	[C]	[B]/[A] [%]	[C]/[A] [%]	[A]−[B]
UGC 3816	205	7	7	3.41	3.41	198
NGC 0384	158	3	4	1.90	2.53	155
NGC 1281	104	8	2	7.69	1.92	96
NGC 1270	168	20	5	11.90	2.98	148
PGC 70520	45	2	1	4.44	2.22	43
NGC 0472	82	0	4	0.00	4.88	82
NGC 2767	83	0	3	0.00	3.61	83
NGC 1271	43	0	1	0.00	2.33	43
UGC 2698	137	33	7	24.09	5.11	104
MRK 1216	120	2	2	1.67	1.67	118
PGC 11179	36	0	2	0.00	5.56	36
PGC 32873	34	0	1	0.00	2.94	34

NOTE—For  $R < 10R_{e,circ}$ 

fits. For the remaining fainter galaxies they adopted a fixed color of  $(g_{475} - z_{850})_0 = 1.16$ . Moreover, Peng et al. (2008) integrated the radial profile of the GCs in each galaxy when counting the number of GCs to prevent overestimating the red GC fraction. We also use the data for effective radii, B-band absolute magnitudes, and stellar masses of the host galaxies in the ACSVCS given by Côté et al. (2004); Ferrarese et al. (2006); Peng et al. (2008). The total number of host galaxies is 100 for the ACSVCS.

We did not include NGC 1399 and NGC 4874 for the comparison with the MCEGs in this study because these two galaxies were not fully covered by the HST images used in this study. They are large galaxies so only their central regions were covered by the HST images used in this study (and previous studies, Blakeslee et al. 2012; Cho et al. 2016): only  $R < 1'.5 \sim 1R_e$  region for NGC 1399 and  $R < 1'.6 \sim 2R_e$  region for NGC 4874. In general, the red GCs in giant ETGs show a stronger central concentration than the blue GCs so the red GC fractions derived from the central region in this study (or previous studies) are larger than the values derived from the entire regions, as used in the sample MCEGs and Virgo galaxies in this study.

In Figure 17(a) we display red GC fractions against effective radii of the host galaxies in our sample of MCEGs, in comparison with the ACSVCS ETGs. Similarly we show red GC fractions against B-band absolute magnitudes and stellar masses of the same galaxies in Figures 17(b) and (c). We also plot NGC 1277 using the value of the red GC fraction given by Beasley et al. (2018). NGC 1277 has a brighter companion galaxy NGC 1278, part of which was covered by the HST/ACS field of NGC 1277. Beasley et al. (2018) subtracted the contamination of NGC 1278 GCs to derive the color distribution of NGC 1277 GCs. Then they derived a

value of the red GC fraction from the  $(g_{475} - z_{850})$  distribution of NGC 1277 GCs using GMM, presenting  $f_{RGC} > 0.83$  (see their Extended Data Figure 4).

Several remarkable features are noted in Figure 17. First, we can divide the Virgo ETGs into two groups according to their sizes: giant ETGs with  $R_e > 5$  kpc and normal/dwarf ETGs with  $R_e < 5$  kpc. Our local MCEGs show similar luminosity or mass with those of giant ETGs while their sizes are similar to those of normal/dwarf ETGs.

Second, the red GC fractions of the MCEGs are larger than those of the giant Virgo ETGs with similar luminosity or mass. The fractions of the MCEGs are also larger than those of the normal/dwarf Virgo ETGs with similar size. We also mark the median of the red GC fractions for the Virgo ETGs along the magnitude and stellar mass, with a magnitude bin of  $\Delta M_B = 1.0$  mag and stellar mass bin of  $\Delta \log(M_*/M_\odot) = 0.5$ . Following the overall trend, we can see that the red GC fractions of the Virgo ETGs increase as their luminosity or mass increase. However, they begin to decrease at  $M_B \approx -20.5$  mag or  $M_* \approx 2 \times 10^{11} M_\odot$  as mentioned in Peng et al. (2008). In contrast, the red GC fractions of our target MCEGs do not decrease even after  $M_B \approx -20.5$  mag or  $M_* \approx 2 \times 10^{11} M_\odot$ .

Third, we can divide the MCEG sample into two subsamples: one for the cluster MCEGs and the other for the group/field MCEGs (field MCEGs hereafter). The cluster MCEG subsample includes five MCEGs, and the field subsample has seven. Note that four out of the five MCEGs in clusters are located very close to the center ( $R < 250$  kpc) of their host clusters, so they are located in a denser environment compared with most galaxies in Virgo. The mean red GC fraction of our 12 MCEG targets is  $f_{RGC} = 0.48 \pm 0.14$ . Interestingly, if we restrict our sample to cluster MCEGs,

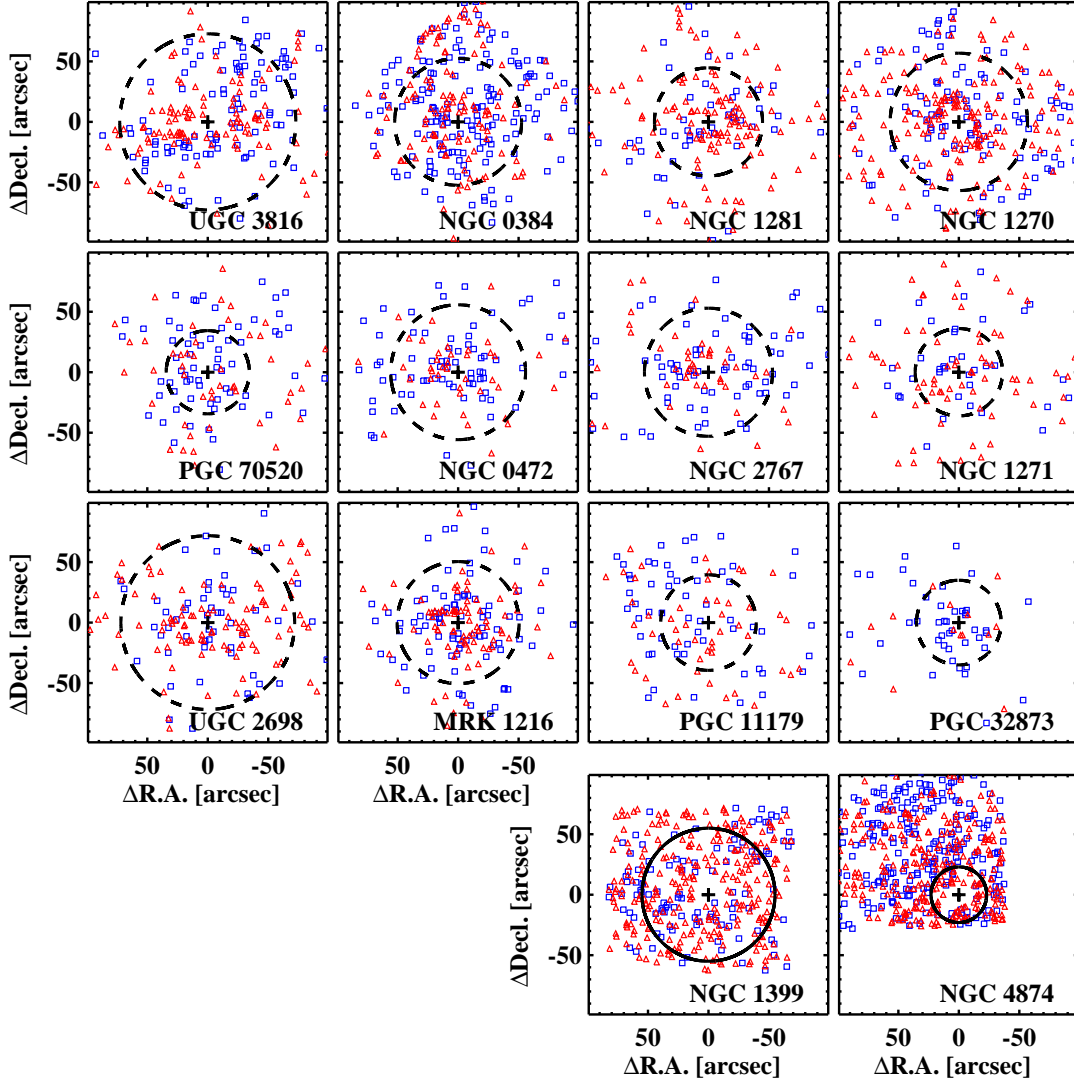


**Figure 14.** Spatial distributions of the bright sources detected in each target MCEG and the two reference galaxies. Blue rectangles and red triangles mark blue and red GCs. Large dashed circles denote  $R = 10R_{e,circ}$  of each galaxy which is a boundary of the GC systems used in this study. For the case of the two reference galaxies, large solid circles denote  $R = 0.5R_e$ .

this value increases to  $f_{RGC} = 0.60 \pm 0.06$ . This value is  $\sim 0.3$  larger than the mean red GC fraction of the giant Virgo ETGs,  $f_{RGC} = 0.33 \pm 0.13$ . If we restrict our sample to field MCEGs, then the mean fraction decreases to  $f_{RGC} = 0.40 \pm 0.10$ . This value is 0.2 lower than the value for the cluster MCEGs, and is similar to the value for the Virgo ETGs. The red GC fraction for normal-size ETGs in the field may be lower than that for cluster ETGs. However, there are no data available for the field normal-size ETGs as homogeneous as those for Virgo galaxies so we could not include them for comparison in this study. These results on red GC fractions are consistent with the previous finding that relic galaxies prefer dense environments. The environmental preference of MCEGs is well summarized in [Beasley et al. \(2018\)](#). In short, local MCEGs, like other normal massive ETGs, prefer dense environments both in observational and

theoretical view (e.g. [Poggianti et al. 2013](#); [Damjanov et al. 2015](#); [Stringer et al. 2015](#); [Peralta de Arriba et al. 2016](#)). If we restrict the area of GC selection for each galaxy to  $R < 5R_{e,circ}$ , the mean red GC fraction does not change much ( $f_{RGC} = 0.51 \pm 0.14$  for all 12 MCEGs,  $f_{RGC} = 0.60 \pm 0.10$  for the cluster MCEGs and  $0.45 \pm 0.13$  for the field MCEGs).

Fourth, the red GC fractions of the MCEGs are not as large as those of NGC 1277. [Beasley et al. \(2018\)](#) obtained  $f_{RGC} > 0.83$  by applying GMM analysis to the  $(g_{475} - z_{850})_0$  color distribution of the NGC 1277 GCs. If we take the result as it is, NGC 1277 can be considered as the unique sample hosting the highest fraction of red GCs. However, there is a possibility that the red GC fractions of our target MCEGs are rather underestimated compared with NGC 1277. In the case of NGC 1277, blue and red GC subpopulations are divided at  $(g_{475} - z_{850})_0 \approx 1.0$  according to the

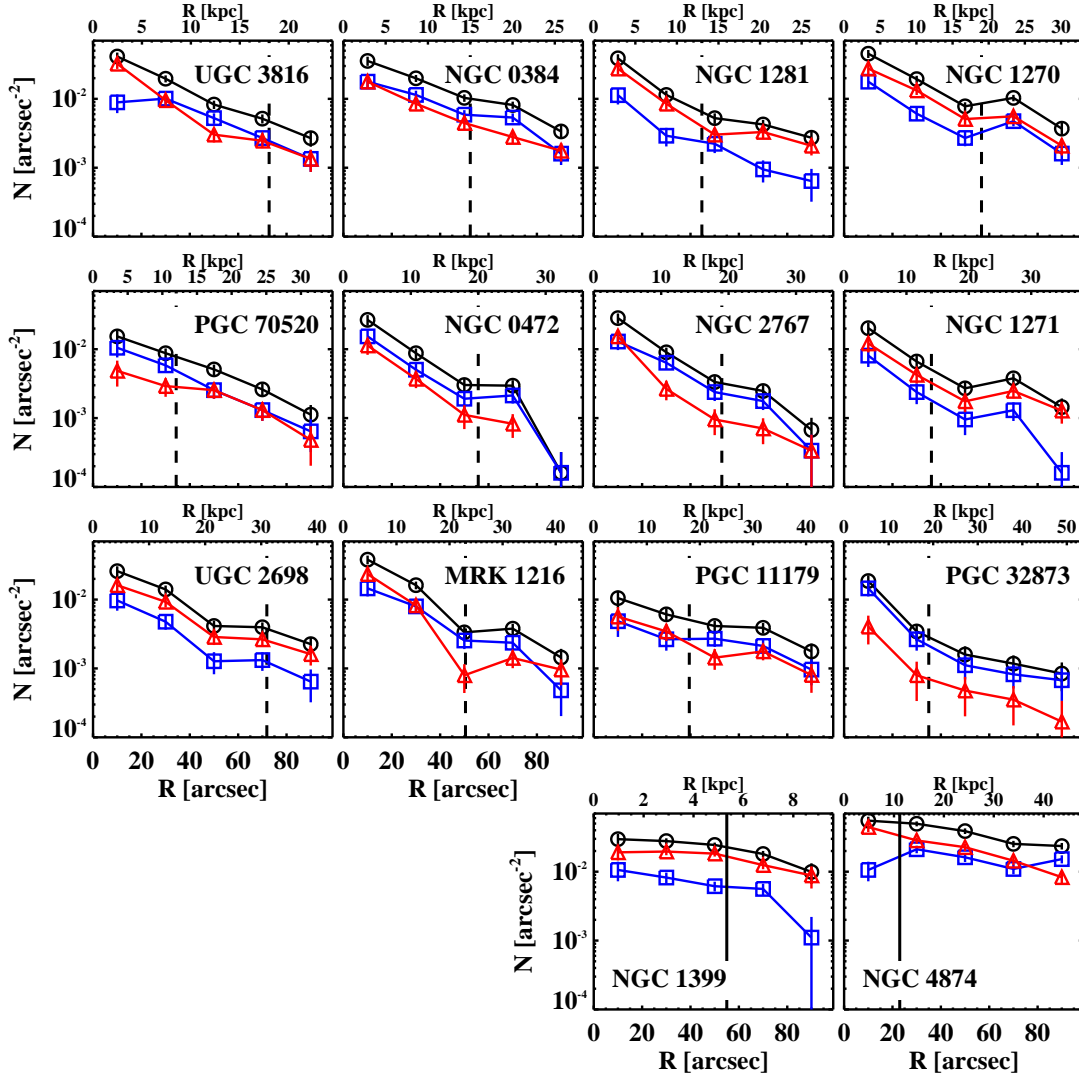


**Figure 15.** Radial number density profiles of the bright sources detected in each target MCEGs and the two reference galaxies. Blue rectangles are profiles of blue GCs, red triangles are profiles of red GCs, and black circles are profiles of all GCs (blue plus red GCs). The dashed lines denote  $R = 10R_{e,circ}$  of each galaxy. For the case of the two reference galaxies, vertical lines denote  $R = 0.5R_e$ .

GMM analysis in Beasley et al. (2018). This color is much bluer than the typical division color,  $(g_{475} - z_{850})_0 = 1.16$ , which was used for the previous studies of the GC color distributions (e.g. ACSVCS ETGs, NGC 1399, and NGC 1278, Peng et al. 2006; Blakeslee et al. 2012; Beasley et al. 2018). Therefore, if we use a fixed color of  $(g_{475} - z_{850})_0 = 1.16$  as in the previous studies to derive the red GC fraction of NGC 1277 instead of using GMM analysis, we obtain a much smaller fraction of  $f_{RGC} = 0.67$  (see Figure 2 or Extended Data Figure 4 in Beasley et al. 2018). This value is similar to the value for NGC 1281 we derived in this study,  $f_{RGC} = 0.70 \pm 0.09$ . Thus, it is possible that the red GC fraction derived from a fixed  $(I_{814} - H_{160})$  color for our sample may be an underestimate compared with NGC 1277. If there is a galaxy such as NGC 1277, hosting a large fraction of red GCs with a blue tail in their color distribution, using a fixed

color can underestimate its red GC fraction. This implies that if we apply GMM analysis to our sample of MCEGs, we may obtain larger red GC fractions similar to NGC 1277. In the case of NGC 1277, there is about 0.2 difference (0.67 and 0.83) in the red GC fraction between the two methods (color cut and GMM). Therefore, the red GC fraction of MCEGs may systematically increase by up to  $\sim 0.2$ . Then NGC 1277 may not be a unique sample anymore.

#### 4.3. Origins of GCs and Relic Galaxies

In this study we find that nearby MCEGs have GC systems dominated by red GCs, and their red GC fractions are on average larger than those of giant ETGs with similar stellar mass or normal/dwarf ETGs with similar size. This result holds significant implications on the origins of GCs and relic galaxies.



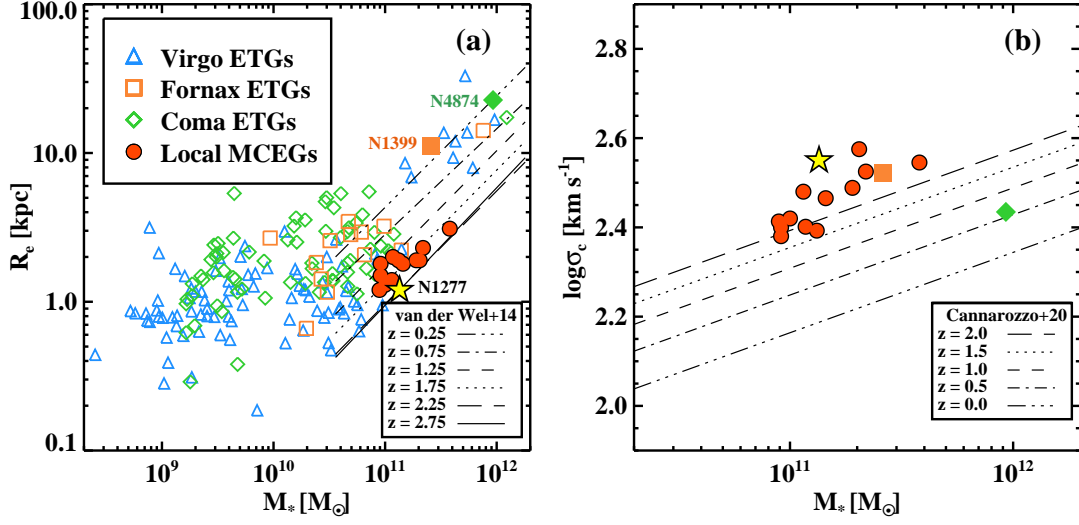


**Figure 16.** (a) Effective radii ( $R_e$ ) vs. stellar masses ( $M_*$ ) for the target MCEGs in this study (filled red circles) in comparison with the Virgo ETGs (blue triangles, Ferrarese et al. 2006; Peng et al. 2008, ACSVCS), the Fornax ETGs (orange squares, Liu et al. 2019, ACSFCS), and the Coma ETGs (green diamonds, Weinzierl et al. 2014, ACS CCS). Filled orange square and filled green diamond denote NGC 1399 and NGC 4874. The yellow star denotes NGC 1277 (Beasley et al. 2018). Black lines are mass-size relations of ETGs at different redshifts (van der Wel et al. 2014). (b) velocity dispersions ( $\log \sigma_c$ ) vs. stellar masses ( $M_*$ ) for the target MCEGs, NGC 1277, and the two reference galaxies. Black lines are mass-velocity dispersion relations of ETGs at different redshifts (Cannarozzo et al. 2020).

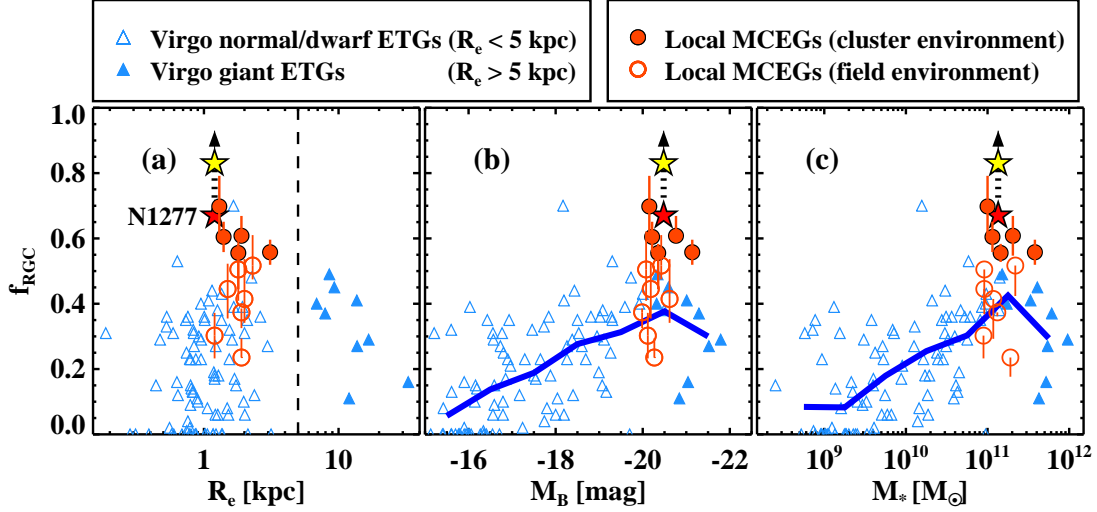


**Figure 17.** Red GC fractions ( $f_{RGC}$ ) vs. (a) effective radii ( $R_e$ ), (b) B-band absolute magnitudes ( $M_B$ ), and (c) stellar masses ( $M_*$ ) for the target MCEGs in this study in comparison with the Virgo ETGs (Côté et al. 2004; Peng et al. 2006, 2008, ACSVCS). Symbols are the same as Figure 16 but we mark the Virgo ETGs with  $R_e > 5$  kpc as filled symbols. Filled red circles mark the MCEGs in cluster environment and open red circles mark the MCEGs in field environment. The yellow star represents the value for NGC 1277 given in Beasley et al. (2018), and the red star denotes the value derived using the fixed color criterion as in this study. The blue solid lines in (b) and (c) represent the median of the red GC fractions for the Virgo ETGs along with the absolute magnitudes and stellar masses.

#### 4.3.1. Origin of Blue and Red GCs

The fraction of metal-rich GCs in local massive galaxies increases from  $\sim 20\%$  to  $\sim 80\%$  as the galactocentric distance decreases from the outer region to the central region (see Fig. 19 in Harris et al. 2017), while the GCs found in the outer halos of local massive ETGs or intracluster regions are mostly metal-poor (Peng et al. 2006; Lee et al. 2010a; Peng et al. 2011; Harris et al. 2017; Forbes & Remus 2018). These results lead to the following scenario on the origin of GCs: Metal-rich GCs are formed either in the central region of massive galaxies during dissipative collapse of their progenitor or in the major merger of massive progenitors. On the other hand, most metal-poor GCs are formed in dwarf galaxies (e.g. Côté et al. 1998; Brodie & Strader 2006; Lee et al. 2010b; Forbes & Remus 2018, and references therein).

In this study we find that most GCs in MCEGs are red GCs (i.e. metal-rich GCs). These red GCs must have originated from the progenitors of the MCEGs rather than from being transferred from other satellite galaxies. Thus, the presence of dominant red GC populations in MCEGs is clear evidence which shows that red GCs are formed mainly in massive galaxies. Very low fraction of blue GCs in MCEGs and very high fractions of blue GCs in the outer region of local massive ETGs imply that the major origin of blue GCs is low mass dwarf galaxies which were accreted to the massive galaxies.

#### 4.3.2. Are Local MCEGs Relic Galaxies?

It is expected that most red nugget galaxies in high density environment (i.e. galaxy clusters or groups) experience many mergers of diverse types during their evolution, and they grow not only in their size and stellar mass but also in their blue GC fraction. In this study we find not only that red GC fractions of the MCEGs in our sample are higher than those of local massive ETGs with similar stellar mass, but also that they are higher than those of local normal/dwarf ETGs with similar size. This implies that the progenitors of the MCEGs became red nugget galaxies of which GC systems are dominated by red GCs about 12 Gyr ago (assuming that they are as old as the metal-rich GCs in the MW, Oliveira et al. 2020), and they must have undergone very few mergers later. They grew little not only in size and stellar mass but also in blue GC fraction. Thus, we conclude that the MCEGs in our sample are genuine relic galaxies.

### 5. SUMMARY AND CONCLUSION

We present a search for GCs in 12 nearby MCEGs, taking advantage of the high resolution HST/WFC3 F814W/F160W images in the archive. The mass-size relation of these MCEGs shows a significant difference from those of local massive ETGs in Virgo, Fornax, and Coma, as shown in Figure 17, but it is consistent with that of red nugget galaxies at

high redshift ( $z \approx 2$ ) (van der Wel et al. 2014; Yıldırım et al. 2017). To see whether these MCEGs host GC systems different from those of local massive ETGs as well, we investigate various photometric properties of the GC systems in these MCEGs. Primary results and conclusion are summarized as follows.

1. CMDs show that most MCEGs host a rich population of GCs. Absolute magnitudes of the detected GCs range from  $M_I \approx -13.0$  to  $-8.5$  mag, the faint limit of which varies on the distance to their host galaxies.
2. Color distributions of the GC candidates with  $I_{814,0} < 25.0$  mag show that most MCEGs show a dominant broad component at  $0.0 < (I_{814} - H_{160})_0 < 1.1$ , which is mainly composed of GCs in each galaxy.
3. We estimate the fraction of red GCs using a fixed color criterion of  $(I_{814} - H_{160})_0 = 0.49 \pm 0.04$ . Red GC fractions of the MCEGs are about 0.2 higher than those of the giant Virgo ETGs with similar stellar mass. Some MCEGs are expected to show comparably large red GC fractions like NGC 1277, a known relic galaxy (Beasley et al. 2018).
4. These results imply that a majority of red GCs were formed early in massive galaxies and that most MCEGs have undergone very few mergers after they became red nuggets about 10 Gyr ago. Thus, it is concluded that they are genuine relic galaxies.

It is expected that more MCEGs will be discovered from new surveys. Recently, Tortora et al. (2018) and Scognamiglio et al. (2020) found 37 new Ultra Compact Massive Galaxies (UCMGs) ( $M_* > 8 \times 10^{10} M_\odot$  and  $R_e < 1.5$  kpc) at  $z < 0.5$  from the Kilo Degree Survey. They combined them with 55 UCMGs from the literature, producing the largest spectroscopically confirmed sample of UCMGs at  $z < 0.5$ . Note that a rich population of GCs was found even in distant galaxy clusters like Abell 2744 at redshift of  $z = 0.308$  from deep HST F814W/F105W images (Lee & Jang 2016b). The UCMGs and new MCEGs at  $z < 0.5$  will be good targets for future studies of their GC systems with HST or JWST. Moreover, follow-up spectroscopic studies for the GCs in the MCEGs with a large telescope (e.g. Keck, GMT, TMT, or eELT) will be helpful to confirm the membership of the GCs and to study their kinematic properties.

## ACKNOWLEDGMENTS

We thank the anonymous referee for useful comments. J.K. was supported by the Global Ph.D. Fellowship Program (NRF-2016H1A2A1907015) of the National Research Foundation (NRF). This work was supported by the NRF funded by the Korean Government (MSIT) (NRF-2019R1A2C2084019). We thank Brian S. Cho for improving the English in the manuscript.

## REFERENCES

- Alamo-Martínez, K. A., Chies-Santos, A. L., Beasley, M. A., et al. 2021, *MNRAS*
- Almaini, O., Wild, V., Maltby, D. T., et al. 2017, *MNRAS*, 472, 1401
- Ashman, K. M., Bird, C. M., & Zepf, S. E. 1994, *AJ*, 108, 2348
- Beasley, M. A., Trujillo, I., Leaman, R., & Montes, M. 2018, *Nature*, 555, 483
- Bertin, E., & Arnouts, S. 1996, *A&AS*, 117, 393
- Blakeslee, J. P., Jordán, A., Mei, S., et al. 2009, *ApJ*, 694, 556
- Blakeslee, J. P., Cho, H., Peng, E. W., et al. 2012, *ApJ*, 746, 88
- NGC 1399
- Bressan, A., Marigo, P., Girardi, L., et al. 2012, *MNRAS*, 427, 127
- Brodie, J. P., & Strader, J. 2006, *ARA&A*, 44, 193
- Cannarozzo, C., Sonnenfeld, A., & Nipoti, C. 2020, *MNRAS*, 498, 1101
- Carter, D., Goudfrooij, P., Mobasher, B., et al. 2008, *ApJS*, 176, 424
- Cho, H., Blakeslee, J. P., Chies-Santos, A. L., et al. 2016, *ApJ*, 822, 95
- Côté, P., Marzke, R.O., & West, M.J. 1998, *ApJ*, 501, 554
- Côté, P., Blakeslee, J. P., Ferrarese, L., et al. 2004, *ApJS*, 153, 223
- Damjanov, I., Zahid, H. J., Geller, M. J., et al. 2015, *ApJ*, 815, 104
- Dekel, A., & Burkert, A. 2014, *MNRAS*, 438, 1870
- Ferrarese, L., Côté, P., Jordán, A., et al. 2006, *ApJS*, 164, 334
- Ferré-Mateu, A., Trujillo, I., Martín-Navarro, I., et al. 2017, *MNRAS*, 467, 1929
- Forbes, D. A., & Remus, R.-S. 2018, *MNRAS*, 479, 4760
- Furlong, M., Bower, R. G., Crain, R. A., et al. 2017, *MNRAS*, 465, 722
- Girardi, L., Groenewegen, M. A. T., Hatziminaoglou, E., et al. 2005, *A&A*, 436, 895
- Gonzaga, S., Hack, W., Fruchter, A., Mack, J., eds. 2012, *The DrizzlePac Handbook*. (Baltimore, STScI)
- Harris, W. E. 2009, *ApJ*, 699, 254
- Harris, W. E., Ciccone, S. M., Eadie, G. M., et al. 2017, *ApJ*, 835, 101
- Illingworth, G. D., Magee, D., Oesch, P. A., et al. 2013, *ApJS*, 209, 6
- Jordán, A., Blakeslee, J. P., Côté, P., et al. 2007, *ApJS*, 169, 213
- Khochfar, S., & Silk, J. 2006, *ApJL*, 648, L21
- Lapi, A., Pantoni, L., Zanisi, L., et al. 2018, *ApJ*, 857, 22
- Lee, M. G., Park, H. S., & Hwang, H. S. 2010, *Science*, 328, 334
- Lee, M. G., Park, H. S., Hwang, H. S., et al. 2010, *ApJ*, 709, 1083
- Lee, M. G., & Jang, I. S. 2016, *ApJ*, 819, 77
- Lee, M. G., & Jang, I. S. 2016, *ApJ*, 831, 108
- Lee, M. G., Kang, J., & Im, M. 2018, *ApJL*, 859, L6
- Lee, M. G., Jang, I. S., & Kang, J. 2019, *ApJ*, in press
- Liu, Y., Peng, E. W., Jordán, A., et al. 2019, *ApJ*, 875, 156
- Muratov, A. L., & Gnedin, O. Y. 2010, *ApJ*, 718, 1266
- Naab, T., & Ostriker, J. P. 2017, *ARA&A*, 55, 59
- Oliveira, R. A. P., Souza, S. O., Kerber, L. O., et al. 2020, *ApJ*, 891, 37
- Oser, L., Ostriker, J. P., Naab, T., Johansson, P. H., & Burkert, A. 2010, *ApJ*, 725, 2312
- Oser, L., Naab, T., Ostriker, J. P., & Johansson, P. H. 2012, *ApJ*, 744, 63
- Peng, E. W., Jordán, A., Côté, P., et al. 2006, *ApJ*, 639, 95
- Peng, E. W., Jordán, A., Côté, P., et al. 2008, *ApJ*, 681, 197
- Peng, E. W., Ferguson, H. C., Goudfrooij, P., et al. 2011, *ApJ*, 730, 23
- Peralta de Arriba, L., Quilis, V., Trujillo, I., et al. 2016, *MNRAS*, 461, 156
- Poggianti, B. M., Calvi, R., Bindoni, D., et al. 2013, *ApJ*, 762, 77
- Schlafly, E. F., & Finkbeiner, D. P. 2011, *ApJ*, 737, 103
- Scognamiglio, D., Tortora, C., Spavone, M., et al. 2020, *ApJ*, 893, 4
- Secker, J. 1995, *PASP*, 107, 496
- Spiniello, C., Tortora, C., D'Ago, G., et al. 2020, *arXiv:2011.05347*
- Stringer, M., Trujillo, I., Dalla Vecchia, C., et al. 2015, *MNRAS*, 449, 2396
- Toft, S., Smolčić, V., Magnelli, B., et al. 2014, *ApJ*, 782, 68
- Toft, S., Zabl, J., Richard, J., et al. 2017, *Nature*, 546, 510
- Tortora, C., Napolitano, N. R., Spavone, M., et al. 2018, *MNRAS*, 481, 4728
- Trujillo, I., Ferré-Mateu, A., Balcells, M., Vazdekis, A., & Sánchez-Blázquez, P. 2014, *ApJL*, 780, L20

- van den Bosch, R. C. E., Gebhardt, K., Gültekin, K., Yıldırım, A.,  
& Walsh, J. L. 2015, *ApJS*, 218, 10
- van der Wel, A., Franx, M., van Dokkum, P. G., et al. 2014, *ApJ*,  
788, 28
- van Dokkum, P. G., Whitaker, K. E., Brammer, G., et al. 2010,  
*ApJ*, 709, 1018
- Weinzirl, T., Jogee, S., Neistein, E., et al. 2014, *MNRAS*, 441,  
3083
- Wellons, S., Torrey, P., Ma, C.-P., et al. 2016, *MNRAS*, 456, 1030
- Yıldırım, A., van den Bosch, R. C. E., van de Ven, G., et al. 2015,  
*MNRAS*, 452, 1792
- Yıldırım, A., van den Bosch, R. C. E., van de Ven, G., et al. 2016,  
*MNRAS*, 456, 538
- Yıldırım, A., van den Bosch, R. C. E., van de Ven, G., et al. 2017,  
*MNRAS*, 468, 4216